Charge-dependent two-particle correlations for unidentified charged particles in Xe-Xe collisions at $\sqrt{s_{NN}} = 5.44$ TeV

Master Thesis

Amber van Keeken

Utrecht University

Supervisor:

Dr. Panos Christakoglou

Utrecht University

Second examiner:

Dr. Marta Verweij

Utrecht University

January 18, 2021

Abstract

Heavy-ion collisions at high energies in the Large Hadron Collider (LHC) create a quark-gluon plasma. The rapid expansion of this medium causes its constituents to experience collective motion. This leaves signatures in the final-state observables, e.g. the transverse momentum distribution and two-particle correlations. In particular, the balance function probes the radial flow by quantifying the two-particle correlation of oppositely-charged particles created at the same point in space and time. The balance function of particles of low transverse momentum shows a dependence on the event multiplicity for heavy-ion collisions, i.e. between gold nuclei (Au-Au) or lead nuclei (Pb-Pb). Recently, this trend was also observed at low transverse momenta in small collision systems such as proton-proton (p-p) or proton-lead (p-Pb) collisions. The origin of the collective effects in these collision systems is still unclear. To bridge the gap in system size, this thesis presents the balance function of unidentified charged particles in collisions between two xenon nuclei (Xe-Xe) with $\sqrt{s_{NN}} = 5.44$ TeV. The results are compatible with smaller collision systems, i.e. p-p and p-Pb, as well as Pb-Pb collisions. This implies that the collective effects are of similar origin in all systems. However, additional studies are needed, in particular on the balance functions for identified charged particles in Xe-Xe.

Contents

Chapter 1

Introduction

According to theoretical calculations [1], at extreme temperatures and densities, a phase transition takes place from normal hadronic matter to a medium where quarks and gluons can move freely. The idea of a quark-gluon plasma (QGP) was proposed in 1975 [2], following results in astrophysics and cosmology of situations where densities are higher than normal nuclear matter, e.g. the centre of neutron stars and the early phases of the universe after the big bang. Though quarks were already commonly believed to make up hadrons, they have never been observed freely. A solution was provided by introducing the idea of quarks moving freely within hadrons, but somehow being confined inside them, making them unable to move as individual quarks at large distances. This was realized in an asymptotically free quantum field theory with a running coupling constant that is big at large distance and small at short distance. This quantum field theory is now known as quantum chromodynamics (QCD) and describes the strong interaction. It uses the SU(3) symmetry and thereby introduces a new quantum number to quarks and gluons, the one of colour. The increasing coupling constant at large distances (small momentum transfer) makes theoretical calculations difficult for quarks in their confined state. Investigating the properties of the quark-gluon plasma provides a unique opportunity to study the fundamental constituents of the theory where they behave as quasi-free particles. It is still thought that a similar phase transition occurred about $10\mu s$ after the Big Bang [3]. Therefore these studies also give insight to the very first moments of the universe.

The properties of the QGP can be studied in heavy-ion collisions, where the collision energy and high density create the necessary conditions for the phase transition. Massive nuclei like gold (Au), lead (Pb) or xenon (Xe) are accelerated to nearly the speed of light and made to collide in accelerators like the Relativistic Heavy-Ion Collider (RHIC) and the Large Hadron Collider (LHC).

One of the important parameters that play a crucial role in the nature of the system created after a heavy-ion collision is the geometry as reflected by what is referred to as *centrality*. The nuclei don't always collide head-on, they can collide with a certain misalignment of their centres, expressed by the impact parameter. Since the impact parameter is not something that can be controlled or measured directly, the collisions, or *events*, are labelled by their centrality. This describes how close to head-on the collision is and is usually expressed in percentiles. A high centrality of 0-5% corresponds to a nearly head-on collision, i.e. an impact parameter close to zero. The most peripheral events have high percentiles, e.g. 80-100%. Figure 1.1 illustrates the relation between the impact parameter and centrality in three different categories: peripheral, mid-central and central events. Centrality can then be determined by other measurements, such as the total number of particles created in the collision, the event *multiplicity*. For central events, the overlap region is larger and more nucleons participate in the collision, resulting in higher multiplicity.

The overlapping region is where a quark-gluon plasma is formed and the remaining parts of the nuclei travel forward. The QGP expands explosively due to high thermal pressure in the centre and is described by relativistic hydrodynamics [4]. This causes the constituents of the medium to expand with an average expansion velocity $\langle \beta_T \rangle$, referred to as *radial flow*. At central collisions and/or higher collision energies, the pressure gradient is larger, leading to a higher expansion velocity. Particles are boosted according to this velocity, on top of their thermal motion, v_{th}, according to

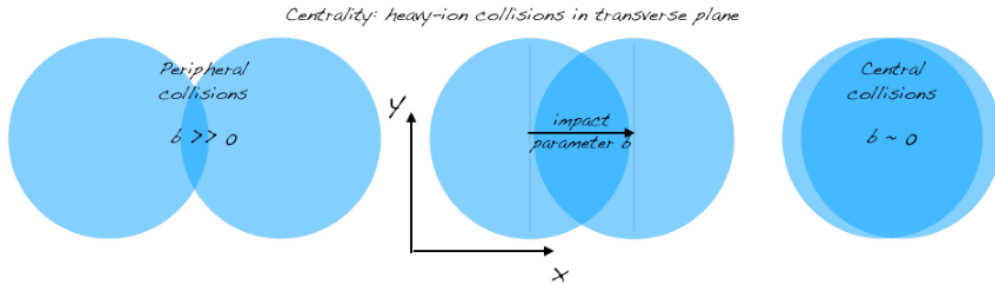$$p_T = \gamma m \langle \beta_T \rangle + v_{\text{th}}, \tag{1.1}$$

Figure 1.1: A schematic illustration of centrality in heavy-ion collisions. Three types of collisions are shown in the plane transverse to the beam axis z: peripheral, semi-central and central, from left to right. The corresponding centrality percentiles could be 80-100%, 50-60% and 0-5%, respectively. The impact parameter b is indicated as the distance between the centres of the nuclei. [5]

where p_T is the transverse momentum of particles with mass m. A larger radial flow should thus be reflected in the p_T spectra of the final particles.

In addition, the shape of the overlap region happens to be reflected in the motion of the final-state hadrons. For non-central events the shape is more elliptic (see Figure 1.1), which leads to a pressure gradient that is larger in the x-direction than in the y-direction. This leads to asymmetric expansion of the medium. Theoretical research concluded that the specific shear viscosity of the QGP is the smallest ever observed ($\eta/s \sim \frac{1}{4\pi}$), meaning it behaves as an ideal fluid, rather than a gas [4]. This allows the initial spatial anisotropies to survive and translate into the final-state momentum distribution. This phenomenon is referred to as *anisotropic flow*.

1.1 Signatures

Studying the quark-gluon plasma has so far focused on indirect methods, since its lifetime is only $\sim 10^{-23}$ s. By studying the final particle distribution one can infer how they were affected by the QGP and with that describe the transport properties of the GQP. This does require a good understanding of the initial particle distribution, which is why a good model for particle production in heavy-ion collisions is also important. Many studies focus on the dependence of QGP signatures on the collision energy or the shape and size of the overlap region. The latter is represented by the event multiplicity or the centrality.

An example of such indirect studies is the measurements of p_T spectra. The spectra of pions, kaons and protons show a shift to higher values when comparing Au-Au collisions at $\sqrt{s_{NN}} = 200$ GeV with Pb-Pb collisions at $\sqrt{s_{NN}} = 2.76$ TeV [6]. This is due to the larger radial flow at the higher energies of Pb-Pb collisions, which gives the particles a momentum boost, as mentioned above. Additionally, it was shown that the expansion velocity depends on the multiplicity of the collision [6]. More central collisions create a larger and longer lived QGP that expands more explosively outwards, leading to a higher expansion velocity.

Other observables used in studying the QGP are the flow coefficients, v_n. The shape of the QGP in non-central events causes elliptic expansion, as mentioned before. Because the medium behaves like an ideal fluid, this spatial ellipticity will translate to an ellipticity in the final momentum distribution. Moreover, since the nuclei consist of nucleons, the overlap region is never as perfectly shaped as shown in Figure 1.1. Instead, the participating nucleons create a shape that fluctuates on each event as illustrated in Figure 1.2. These spatial anisotropies will also translate to higher order anisotropies (e.g. triangular or rectangular) in the momentum distribution of the final particles [7]. These patterns of anisotropic flow can be quantified using a Fourier expansion of the event averaged azimuthal particle distribution:

$$\frac{\mathrm{d}N}{\mathrm{d}\varphi} \propto 1 + 2\sum_{n=1}^{\inf} v_n e^{in(\varphi - \Phi_n)}, \tag{1.2}$$

where $v_n = \langle \cos n(\varphi - \Phi_n) \rangle$ are the anisotropic-flow coefficients and Φ_n is the corresponding flow symmetry plane. However, since these planes are not accessible in the experiment, the v_n coefficients are estimated using
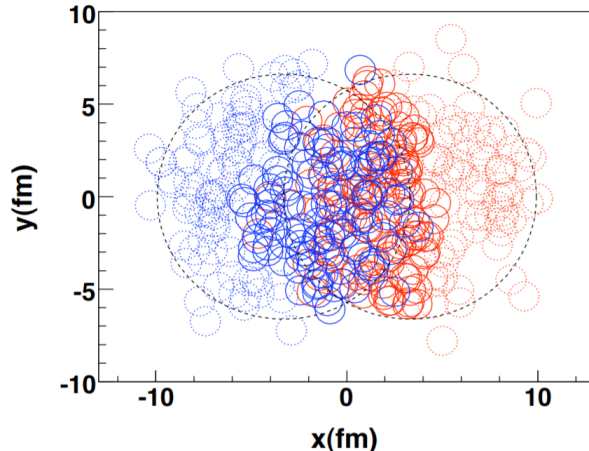
Figure 1.2: Illustration of the participating nucleons in a Pb-Pb collision, indicated by the solid circles. The spectator nucleons are dashed. The participating nucleons fluctuate in number and overall shape event by event. [11]

two-particle or multi-particle correlations [8]. The second Fourier coefficient v_2 is the dominant harmonic and reflects the initial elliptic geometry of the collision. It has indeed been shown for many systems, that v_2 is larger for non-central events, where the initial spatial ellipticity is larger [9, 10]. In particular, Figure 1.3 shows the elliptic and triangular flow coefficients from Xe-Xe collisions compared with Pb-Pb collisions. Not only do both collision systems show the expected centrality dependence, a difference between xenon and lead is observed that is due to the deformation of the xenon nucleus. Both are shown to be well described by hydrodynamic models. This is still a very interesting field since these flow harmonics are sensitive to the specific shear viscosity, as mentioned before, and can therefore be used to study the QGP transport properties, especially when combined with model expectations. Overviews of the current findings are available, e.g. in Ref. [8].

Another way to obtain information about the QGP is to study the interaction of highly energetic (hard) partons with the medium. These partons fragment into many particles in a small region, a *jet*. Though these do not experience the collective motion of the quark-gluon plasma, they do lose energy due to interaction with the medium. This leads to a suppression relative to the case where no QGP is formed of high-p_T particles and jets in the final state. This phenomenon is called *jet quenching*. The observable used to quantify this is the nuclear modification factor R_{AA}. It is measured as the ratio of hadron yields measured in heavy-ion collisions over the expected yield of the superposition of the corresponding number of nucleon-nucleon collisions, scaled accordingly to account for the bigger size of the ions relative to protons:

$$R_{\mathrm{AA}}(p_T) = \frac{\mathrm{d}N_{\mathrm{h}}^{\mathrm{AA}}(p_T)/\mathrm{d}p_T}{\langle N_{\mathrm{coll}}\rangle \mathrm{d}N_h^{\mathrm{pp}}(p_T)/\mathrm{d}p_T} \tag{1.3}$$

If $R_{AA} = 1$, then one would conclude that there are no final-state effects affecting the spectrum. As seen in Figure 1.4a for many measurements the R_{AA} is well below one [12]. This indicates a large suppression of the high-energy partons in heavy-ion collisions relative to the scaled p-p reference. These results support the hypothesis of significant interactions between high-energy partons within a dense medium created in heavy-ion collisions. Furthermore, as seen in Figure 1.4b, the suppression for peripheral events is much less. This can be understood by the fact that the medium created is smaller in size, lifetime and density, leading to an overall smaller energy loss [13].

Finally, the medium and its properties can also be studied with angular-correlation techniques, the most well known of which involves two particles and is thus referred to as the two-particle correlations method. These studies measure the distribution of the separation between two particles in both pseudo-rapidity and azimuthal angle, $(\Delta\eta, \Delta\varphi)$, further discussed in Section 2.2.4. A correlation function for charged particles is also defined later in Equation 3.2. Studies in Au-Au and Pb-Pb show distinct features [14, 15], which
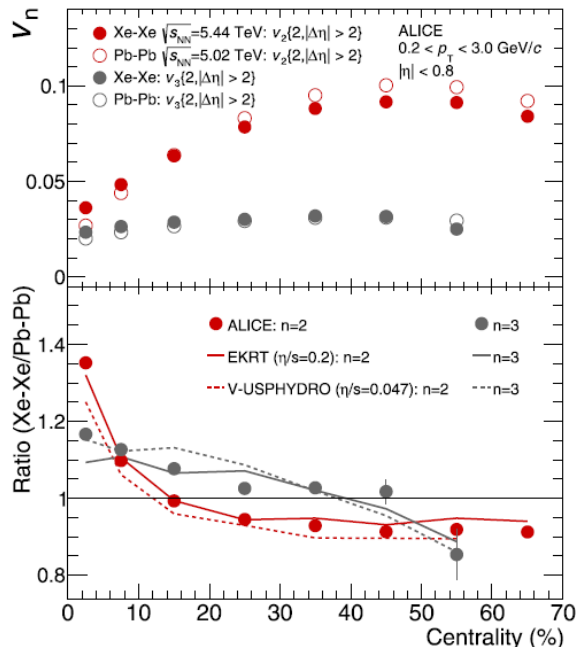
Figure 1.3: Comparisons of charged particle $v_n\{2\}$ integrated over $0.2 < p_T < 3.0$ GeV/c as a function of centrality from Xe-Xe and Pb-Pb collisions (top panel). The corresponding ratios (Xe-Xe/Pb-Pb) are compared to hydrodynamical model predictions (bottom panel). Adapted from [9].

can be seen in Figure 1.5. The correlations caused by particles from different jets are reflected in a ridge at $\Delta\varphi = \pi$, from back-to-back topologies, while a peak around $(\Delta\eta, \Delta\varphi) \approx (0, 0)$ emerges from particles within the same jet. Additionally, a *near-side ridge* is seen around $\Delta\varphi = 0$ that extends in $\Delta\eta$. While its origin was subject of theoretical debate, it is now believed to be associated with anisotropic flow [16].

Crucial for this conclusion was local charge conservation. This is probed by the balance function that quantifies the correlation between two oppositely charged particles created at the same location in space and time. It was proposed to be sensitive to the hadronization time of the quark-gluon plasma [17]. The first study was done on Au-Au collisions at $\sqrt{s_{NN}} = 130$ GeV by the STAR collaboration [18] and showed that the balance function was narrower when the ions collide head-on than for peripheral collisions. Subsequent studies on Pb-Pb were performed at the much higher energy of the LHC concluded the same, but only for particles with low transverse momentum ($p_T < 2$ GeV) as shown in Figure 1.6. Studying different collision systems at various collision energies can help shed light on the role of the initial energy density and the production mechanism of the final-state particles.

1.2 Small collision systems

Recently, signatures of the QGP have been observed in smaller collision systems, i.e. proton-proton collisions and proton-lead collisions. The elliptic flow was shown to be of the same order as the one measured in low-multiplicity heavy-ion collisions [10], the near-side ridge was observed [19] and balance functions showed features similar to the heavier collision systems as well, see Figure 1.6 [20, 21]. The origin of these collective effects is still unclear. It raises the question whether a small QGP is formed even in these collisions where the energy density formed might be much lower due to the smaller size of the colliding objects.

In particular, studies on the balance function of p-p collisions show a dependence on multiplicity only expected in heavy-ion collisions where it is attributed to radial flow [20, 21]. Figure 1.6 illustrates the similarity of the results of the small systems compared with Pb-Pb. As in the heavier systems, the multiplicity dependence is only observed for low-p_T particles. Some of the findings will be mentioned in the following chapters, where the balance function is discussed in more detail.
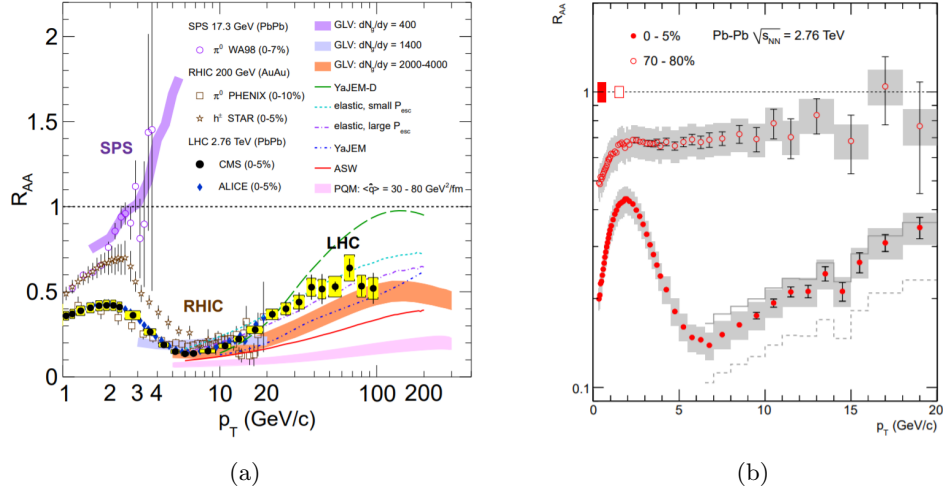
Figure 1.4: (a) Measurements of the nuclear modification factor R_{AA} in central heavy-ion collisions at three different centre-of-mass energies, as a function of p_T, for neutral pions, charged hadrons, and charged particles, compared to several theoretical predictions (see [12]). (b) The nuclear modification factor for Pb-Pb collisions at $\sqrt{s_{NN}} = 2.76$ TeV, for central (0-5%) and peripheral (70-80%) collisions [13].
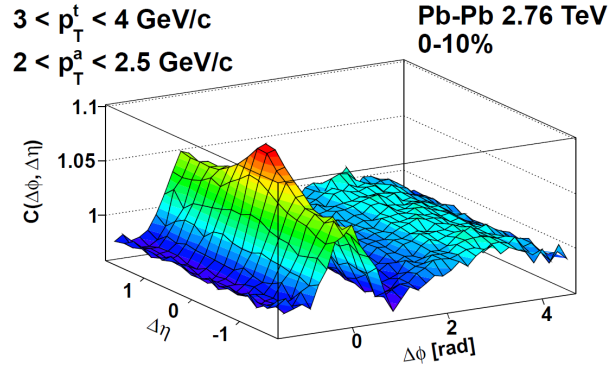

Figure 1.5: An example of a two-particle correlation function $C(\Delta\eta, \Delta\varphi)$ at low to intermediate transverse momentum for central Pb-Pb collisions at $\sqrt{s_{NN}} = 2.76$ TeV. [15]

The study presented in this document will measure the balance function for charged particles in collisions between two xenon (Xe) ions at $\sqrt{s_{NN}} = 5.44$ TeV. These nuclei have A = 129 and are thus similar to lead (A = 208). The balance function will be calculated for unidentified charged particles with $0.2 < p_T < 2.0$ GeV. The results will be compared to other collision systems, as well as model expectations, with the goal of gaining a better understanding of the origin of collective effects in heavy-ion collisions and small collision systems.
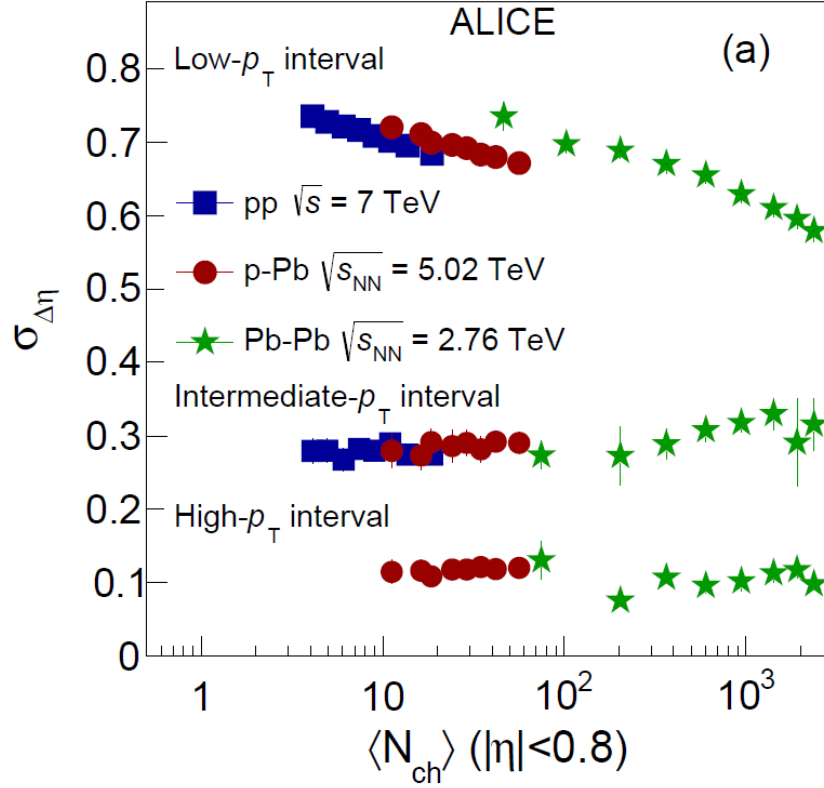
Figure 1.6: The width of the balance function in $\Delta\eta$ for the three systems analyzed (pp, p–Pb and Pb–Pb), as a function of the charged-particle multiplicity, estimated with the V0A for $|h| < 0.8$. The low-, intermediate-, and high-p_T intervals correspond to $0.2 < p_{T,assoc} < p_{T,trig} < 2.0$ GeV/c, $2.0 < p_{T,assoc} < 3.0 < p_{T,trig} < 4.0$ GeV/c, and $3.0 < p_{T,assoc} < 8.0 < p_{T,trig} < 15.0$ GeV/c, respectively.[20]

Chapter 2

The Detector

2.1 The Large Hadron Collider

To investigate the inner structure of particles and examine a medium such as the quark-gluon plasma, one needs to collide heavy composite particles at high energies. The Large Hadron Collider (LHC) at CERN in Geneva, does exactly this. It is currently the world's largest and most powerful particle accelerator. It can accelerate protons up to 7 TeV. The LHC uses a 27 km underground ring of tunnels, where particles are guided through two beam pipes in opposite directions. The particles are accelerated by electric fields and bent to stay in a circular path by superconducting electromagnets. The two beams are made to intersect at four collision points, each surrounded by one of the four largest detector experiments: ATLAS, CMS, ALICE and LHCb. Each detector consists of different layers of detection technology to be able to detect, identify and measure the energy of the particles created in a collision. While ATLAS and CMS are general-purpose detectors, LHCb focuses on studies that probe the asymmetry between matter and antimatter and the ALICE detector focuses on studying the quark-gluon plasma.
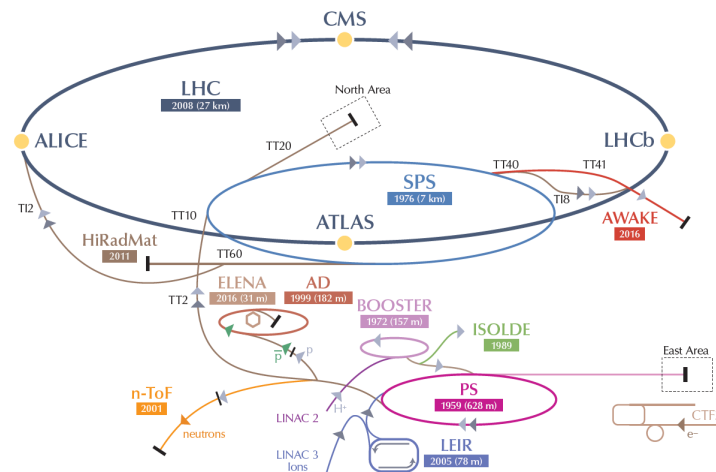
Figure 2.1: Schematic overview of the LHC at CERN in Geneva, including the preliminary accelerating structures and the four largest detectors ATLAS, CMS, LHCb and ALICE [22].

2.2 ALICE

The name ALICE stands for A Large Ion Collider Experiment and consists of 18 sub-detectors, as seen in Figure 2.2, specifically designed to detect, track and measure the many-particle system created in a heavy-ion collision. Most of the work in tracking the particles is done in the Inner Tracking System (ITS) and the Time

Projection Chamber (TPC), which are closest to the interaction point. Particles are identified by combining the ITS and TPC with the Time of Flight detector (TOF). These detectors will be described in more detail below. Essential for this identification is the use of a magnetic field, which curves the trajectory of charged particles according to their charge and momentum. The central barrel of the ALICE detector, is situated inside a solenoid magnet, shown encased in red in Figure 2.2. Muons are identified by a separate detector: the muon spectrometer, seen on the right in Figure 2.2, on the C-side or muon-side. An absorber stops all other particles from reaching the muon trackers. The HMPID and TRD identify high-momentum hadrons and electrons respectively and photons are detected by the PHOS, the PMD in the forward direction and the EMCal. This ElectroMagnetic Calorimeter is used to measure jets and in particular the jet-quenching effects that occur due to the QGP, as mentioned before. Finally, the time of the collision is determined by the T0 detector and the centrality of the event is determined by the V0 detectors, the FMD and ZDCs. The centrality of the event is especially important when investigating the quark-gluon plasma. As described in the previous chapter, the shape and size of the QGP depends on the centrality of the collision. The centrality is strongly correlated to the multiplicity, the amount of particles generated in an event. These are often indicated as a percentile, rather than an absolute number of particles, where "0-5%" means the 5% of events where the multiplicity was the highest (which corresponds to the most central events, i.e. the most amount of overlap.[1]) To determine the multiplicity percentile, the V0 detectors on either side of the interaction point are used. These scintillator counters are also used as a minimum-bias trigger (together with the SPD). The Forward Multiplicity Detector (FMD) also provides multiplicity information and the Zero Degrees Calorimeters (ZDCs) determine the centrality of the event by measuring the energy carried by the non-participating nucleons, 116 m away from the interaction point. For a detailed description of all the sub-detectors of ALICE, see [23]. The sub-detectors relevant to this analysis are described in more detail below.
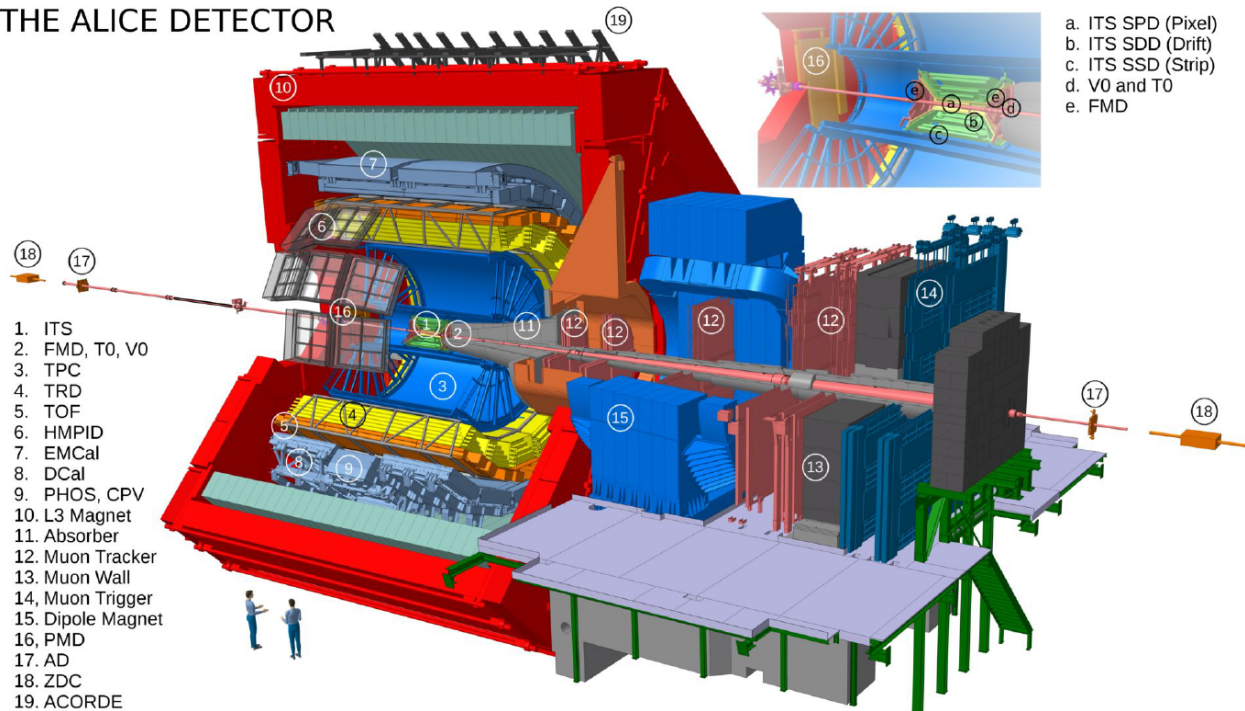

Figure 2.2: Overview of the sub-detectors of the ALICE detector, A Large Ion Collider Experiment at the LHC at CERN.

---

[1]This can get confusing, since the largest centrality is sometimes described with a high percentage, e.g. 90-100%, referring to the amount of 'overlap' in the collision.
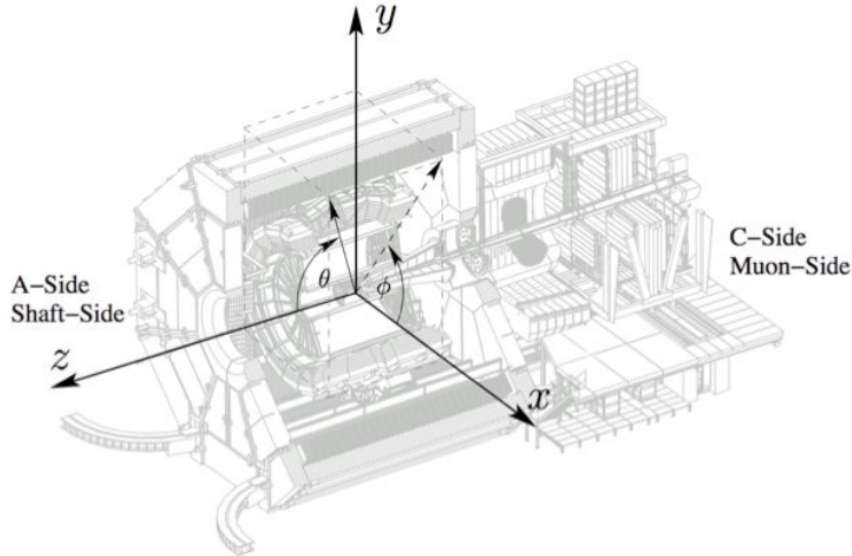
Figure 2.3: Coordinate system used for the ALICE detector analysis. With the z-axis pointing towards ATLAS, the x-axis pointing towards the center of the LHC and the y-axis upwards. The azimuthal angle φ and the polar angle θ are indicated.

2.2.1 ITS

The Inner Tracking System (ITS) is at the center of the ALICE detector and is closest to the interaction point where the collisions take place. It consists of two layers of Silicon Pixel Detectors (SPD), two layers of Silicon Drift Detectors (SDD) and two layers of Silicon Strip Detectors (SDD). These detect any particles with a charge that passes through. The SPD is used together with the V0 detector as a minimum-bias trigger. The ITS has the important task of determining the primary vertex, the exact position of the collision. Based on this, particles that seem to come from somewhere else are rejected, as they have not been created in the collision. Particle tracks are reconstructed by fitting a curve from the signal clusters in the TPC, back through the clusters in the ITS.[2] This can be extrapolated back towards the interaction point to determine the Distance of Closest Approach (DCA) to the primary vertex. One can then set a maximum to this DCA and have tracks that exceed this value be discarded.

2.2.2 TPC

Since the inner tracking system only covers a small part of a particle's trajectory, the next layer of the detector continue to track it. The Time Projection Chamber (TPC) will measure up to 159 points of the trajectory for each particle. Since these main parts of the detector (the 'central barrel') are placed inside a magnet, the particles will bend while traversing the detector. The amount of curvature provides the charge and momentum of a particle. The TPC consists of a cylindrical chamber with two readout plates at the ends. The inner radius of the cylinder is 85cm and the outer radius is 250cm [23]. This volume is filled with a gas that is ionized where a charged particle passes through. The freed electrons are drifted to a point in (r, φ) on one of the readout plates by an electric field and the time it takes to get there is used to determine the z-coordinate.

2.2.3 TOF

To identify the particles, the Time-Of-Flight (TOF) detector determines the time it takes a particle to reach it from the primary vertex. The starting time at the primary vertex is determined by T0. Together with the

---

[2]This is a simplification, in fact, the track is formed by three steps of fitting and filtering, going inwards, outwards and inwards again to get the most accurate trajectory [23].

momentum, the velocity gives us the mass and thus identity of a particle. The TOF covers the area around the beam pipe at a radius of 370cm to 399cm. It consists of a system of 1638 MRPC strips. These Multi-gap Resistive-Plate Chambers use a high electric field and are filled with a gas, so that any ionisation by a traversing charged particle creates a gas avalanche process that generates a signal on the pick-up electrodes [23].

2.2.4 Coordinates

The coordinate system used in the ALICE collaboration is shown in Figure 2.3. The z-axis is chosen to be along the beam pipe, sometimes called the 'forward' direction, with positive z on the A-side (towards the ATLAS detector) and negative on the C-side (towards CMS). The x-axis is chosen to point towards the center of the LHC and the y-axis points upwards to form a right-handed coordinate system. The azimuthal angle φ and the polar angle θ are defined as usual and are used to describe the position of a particle in the detector, rather than the Cartesian coordinates. Instead of θ, a related quantity called the pseudo-rapidity η is used to describe the position of a particle with respect to the beam axis. It is defined as

$$\eta = -\ln[\tan(\theta/2)] \tag{2.1}$$

and ranges from 0 at the y-axis to infinity at the z-axis. It is an approximation for the rapidity y that holds for highly relativistic particles. The actual rapidity is defined as:

$$y = \frac{1}{2}\ln\left(\frac{E + p_z c}{E - p_z c}\right) = \ln\left(\frac{E + p_z c}{\sqrt{m^2 c^4 + p_T^2 c^2}}\right), \tag{2.2}$$

where p_T is the momentum transverse to the beam axis. It is used often in particle physics because of the Lorentz-invariant nature of the difference of two rapidities, which simplifies calculations and makes it easier to compare systems. However, since the total energy and mass is needed, it is hard to measure, which is why the pseudo-rapidity is used. It then makes sense to describe the coverage of different detectors in this quantity η instead of Cartesian coordinates, to immediately get a sense of which type of particles it can detect. The central barrel of the ALICE detector covers the range $|\eta| < 0.9$. While the muon spectrometer, for example, detects muons in the region $-4.0 < \eta < -2.5$.

Chapter 3

The Balance Function

The balance function is used as a measure of the collective motion of the system after a heavy-ion collision. When first introduced, it was proposed to determine at what stage quark production took place [17]. The earlier a charge/anti-charge pair is created, the further it can separate in rapidity. The balance function quantifies the correlation in pseudo-rapidity (η) and azimuthal angle (φ) of oppositely charged particle pairs created in the same location in space and time. It is also believed to be a sensitive probe of the radial flow of the system [24]. The balance function is defined as

$$B(\Delta\eta, \Delta\varphi) = \frac{1}{2}[c_{(+,-)} + c_{(-,+)} - c_{(+,+)} - c_{(-,-)}]. \tag{3.1}$$

In the previous equation, the correlation functions $c_{(a,b)}$ are distributions of particle pairs, normalized to the number of *trigger* particles, as explained below, for different charge combinations.

The correlation functions for the different charge combinations are based on the per-trigger yields and defined as

$$c_{(+,-)} = \frac{1}{N_{trig,+}} \frac{d^2 N_{assoc,-}}{d\Delta\eta d\Delta\varphi} = \frac{S_{(+,-)}}{f_{(+,-)}} \equiv \frac{SE_{(+,-)}}{ME_{(+,-)}}, \tag{3.2}$$

for the combination of a positive trigger particle and a negative associated particle and similarly for the other charge combinations. Here the signal is defined as

$$S_{(+,-)} = \frac{1}{N_{trig,+}} \frac{d^2 N_{same,(+,-)}}{d\Delta\eta d\Delta\varphi} \equiv SE_{(+,-)} \tag{3.3}$$

and the background as

$$f_{(+,-)} = \alpha \frac{d^2 N_{mixed,(+,-)}}{d\Delta\eta d\Delta\varphi} \equiv ME_{(+,-)}, \tag{3.4}$$

where α is a normalisation factor, as explained below [20]. SE and ME refer to the procedure of counting pairs within the same event and with what is called the event-mixing technique, respectively. Both will be explained below. Let's describe what exactly happens in the analysis. For the $(+, -)$ charge combination, one of the positively charged particles in an event is taken as the *trigger* particle. This particle is paired with each of the negatively charged particles in the same event (SE), an *associated* particle, until all combinations are made. For each pair the p_T of both particles and the angular separation between the particles in $(\Delta\eta, \Delta\varphi)$ is stored in a multi-dimensional histogram. For this analysis, only pairs with transverse momenta in the range $0.2 < p_T < 2.0$ GeV/c are used, resulting in a two-dimensional histogram, the distribution $d^2 N_{same,(+,-)}/d\Delta\eta d\Delta\varphi$. This distribution and $N_{trig,+}$ are summed separately over all events before computing $S_{(+,-)}$. An example of this distribution in this analysis is shown in Figure 3.1a. It is hard to discern any physics from this, as it is dominated by the background.

To determine this background, a similar distribution is made. Each trigger particle is paired with associated particles from at least 5 other events to get the Mixed-Event (ME) background distribution. Events are mixed when they have the same multiplicity class and a V_z within ± 2 cm, where V_z is the position of the primary vertex along the beam axis. In this analysis a maximum of 15 mixing events was used to limit the

(a) SE   (b) ME
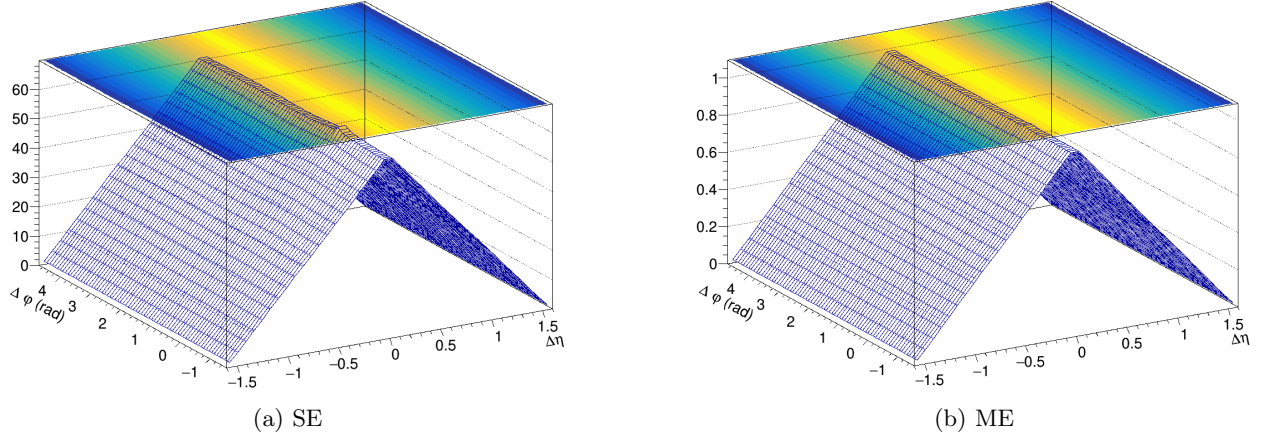
Figure 3.1: The same-event (SE) and mixed-event (ME) per-trigger yields of the $(+,-)$ charge combination for 5-10% multiplicity in Xe-Xe $\sqrt{s_{NN}} = 5.44$ TeV.
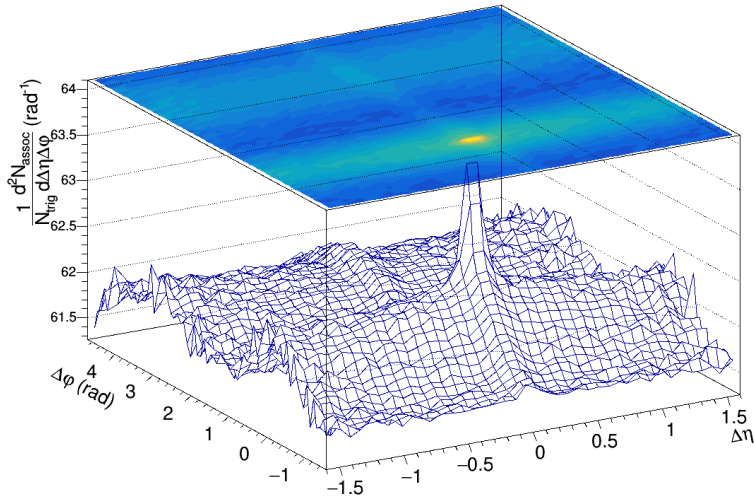

Figure 3.2: The correlation function $c_{(+,-)}$ for the 5-10% multiplicity class in Xe-Xe $\sqrt{s_{NN}} = 5.44$ TeV.

computational time needed to built the background function. An example of the mixed-event distribution for the $(+,-)$ charge combination is shown in Figure 3.1b. This distribution is already normalized to the value of $d^2 N_{mixed,(+,-)}/d\Delta\eta d\Delta\varphi$ at $\Delta\eta = 0$, represented by α in equation 3.4. This way the mixing of events corrects for the detector *acceptance*; the probability of detecting both particles in a pair, depending on their separation $(\Delta\eta, \Delta\varphi)$. It is highest at $\Delta\eta = 0$, where both particles face the same detector conditions. As the relative pseudo-rapidity difference increases, the probability of detecting both particles decreases, since it is more likely for one or both of the particles to fly out of range of the central barrel of the ALICE detector [25].

After dividing the two distributions as shown in equation 3.2, the correlation function for the $(+,-)$ charge combination looks like Figure 3.2. Now clear structures in the particle-pair separation can be seen.

By subtracting the same charge combinations as shown in equation 3.1, it is ensured that the two particles are created at the same location in space and time. The factor $\frac{1}{2}$ makes sure the integral of the balance function is normalized to unity, representing charge conservation [17]. When integrating over pseudo-rapidity
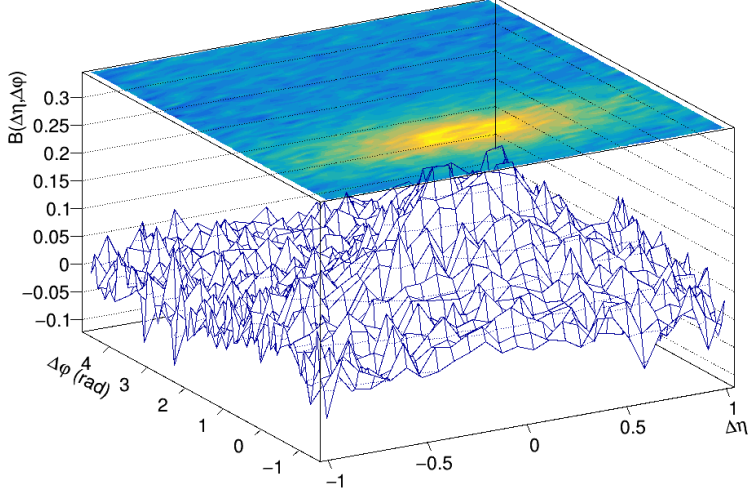
Figure 3.3: The balance function $B(\Delta\eta, \Delta\varphi)$ for the 5-10% multiplicity class in Xe-Xe $\sqrt{s_{NN}} = 5.44$ TeV.

and azimuthal angle, we recover all particle pairs and get:

$$\sum_{\Delta\eta, \Delta\varphi} B = \frac{1}{2}\left[\frac{N_+ N_-}{N_+} + \frac{N_- N_+}{N_-} - \frac{N_+(N_+ - 1)}{N_+} - \frac{N_-(N_- - 1)}{N_+}\right]$$

$$= \frac{1}{2}[N_- + N_+ - (N_+ - 1) - (N_- - 1)] = 1, \tag{3.5}$$

where N_+ and N_- are the average number of positive and negative particles, respectively. Note that a trigger particle is not matched to itself when forming pairs.

Once the balance function distribution is computed by adding and subtracting the histograms of the different charge combinations, it looks like Figure 3.3 (for high multiplicities). The majority of the correlations is concentrated around $(\Delta\eta, \Delta\varphi) = (0,0)$, indicating that balancing pairs are predominantly emitted very close in phase space. The shape of the balance function will be discussed in detail in the results.

The balance function is then projected separately onto $\Delta\eta$ and $\Delta\varphi$. The projection onto $\Delta\eta$ is done only for the near side ($-\pi/2 < \Delta\varphi < \pi/2$). From the one-dimensional plots the widths $\sigma_{\Delta\eta}$ and $\sigma_{\Delta\varphi}$ are determined by computing the standard deviation. The uncertainty in these widths is computed by randomly smearing each point in the balance function projections following a Gaussian function centered around the value at that point with a sigma that is the statistical uncertainty of that point. For each of the 10000 smeared distributions a new width is computed. From these 10000 values a standard deviation is then computed which is used as the statistical uncertainty on the measured width ($\sigma_{\Delta\eta}$ and $\sigma_{\Delta\varphi}$). The balance function is also integrated, using the $\Delta\varphi$ projection. This *yield* is computed for the near side ($-\pi/2 < \Delta\varphi < \pi/2$), the away side ($\pi/2 < \Delta\varphi < 3\pi/2$) and the total distribution separately. A similar smearing procedure is used to compute the statistical uncertainties in the yields.

The widths and yields are determined for each centrality or multiplicity class, to get insight in the evolution of the width of the balance function with growing centrality. The resulting two plots are the width in either $\Delta\eta$ or $\Delta\varphi$ over the multiplicity class. How the multiplicity of an event is determined is described in Section 4.3.

Chapter 4

Analysis details

4.1 Data sample and selection

The analysis presented in this document was performed on Xe-Xe collision data at $\sqrt{s_{NN}} = 5.02$ TeV collected with the ALICE detector in 2017 during LHC Run2. The data sample that was used is recorded as LHC17n. It contains only two runs with ~ 4.5 million events.

Events were selected by imposing several requirements. First of all, the kINT7 online minimum-bias trigger was used, which requires a signal in both VZERO detectors. To reject events coming from overlapping collisions, *pile-up*, the default MultiVertex method uses tracks to determine the primary vertex and tag tracks pointing to the wrong vertex. The position of the primary vertex, V_z, can vary along the beam axis (z). Only events where the primary vertex was within 10 cm of the interaction point were selected. After applying all the selection criteria, approximately 1.4 million events were analyzed.

Standard cuts were applied on tracks reconstructed by the ITS and TPC [26]. To select high-quality tracks, tracks were required to have at least 70 detected cluster in the TPS. The maximum χ^2 of the track fit per cluster in the TPC was set to 4. Finally, one signal was required in either the SPD or SDD layer of the ITS. Additionally, tight cuts were applied based on the distance of closest approach (DCA) of the track to the primary vertex to reduce the contamination of secondaries. Tracks were only selected when they passed a tight p_T-dependent requirement $\mathrm{DCA_{xy}} < 0.0105 + 0.0350/p_T$ cm in the transverse direction and $\mathrm{DCA_z} < 2$ cm in the longitudinal direction.

4.2 Corrections

The detector is not perfect. It has a limited efficiency, since not the entire area around the interaction point is covered by active material. The detectors are connected by pieces of metal and readout strips through which particles can escape undetected. Moreover, some parts of the detector could be defective, providing more 'dead' area. The acceptance of the detector is also limited. When doing analyses on two-particle correlations, there is a possibility that only one particle of a pair is detected, due to the limited $\Delta\eta$ range of the detector. Finally, there are contaminations. Not every particle that is detected comes from the collision. They can originate from radioactive material inside the detector, interactions with the detector material or from outside sources.

We need to correct for these imperfections and contaminations. The effects are estimated by performing a Monte Carlo simulation that mimics the generation of particles and the response of the ALICE detector. This uses the exact same configuration of the detector as the data, e.g. any non-working channels and the strength of the magnetic field. The Monte Carlo simulation generates particles based on the collision values, using HIJING [27] and then simulates the response of the ALICE detector with GEANT3 [28]. By comparing the particles created in the collision generator to the particles measured by the simulated detector, a correction factor can be computed, with which actual collected data can be multiplied to recover the amount of particles actually produced by the collision.
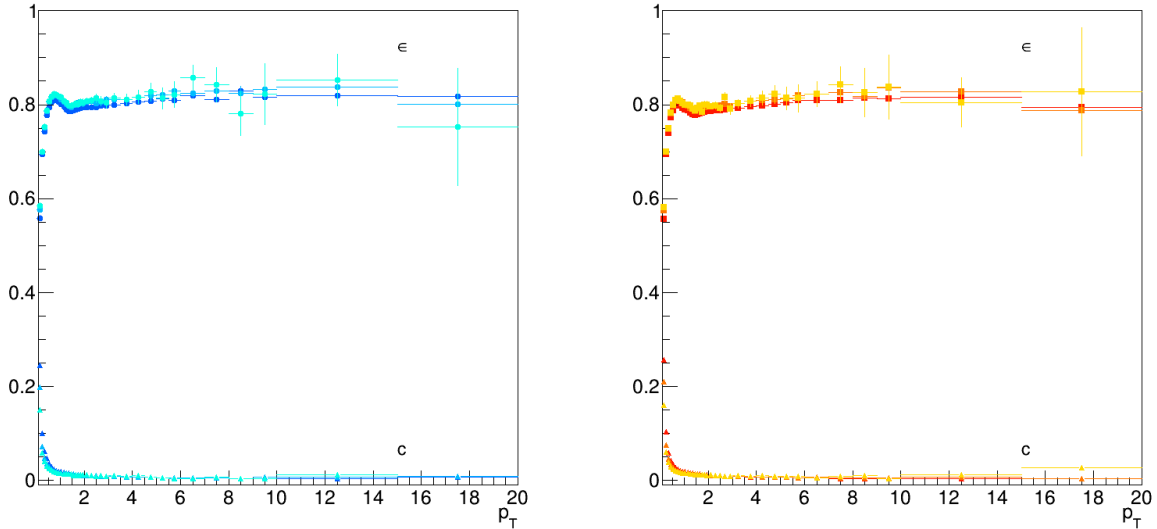
Figure 4.1: The efficiency (ϵ) and contamination (c) factors. The factors were computed for positive (left) and negative (right) particles separately. The contamination factors are shown at the bottom of the plot and the efficiency is shown above. Both are plotted for the 0-5%, 30-40% and 70-80% multiplicity classes, where darker colours correspond with higher multiplicity.

This single-particle correction factor is a function of p_T and is defined as

$$w(p_T) = \frac{1-c}{\epsilon}, \tag{4.1}$$

where both the efficiency ϵ and the contamination from secondary tracks c depend on the transverse momentum. When computing the signal and background of the correlation functions, each term is corrected with this correction factor. The efficiency is computed as the number of reconstructed tracks divided by the number of generated particles. The contamination is defined as the number of secondary tracks, coming from weak decay or interaction with the material, divided by the total number of generated particles (primaries and secondaries). Both can be seen in Figure 4.1 for three different multiplicity classes, for positively and negatively charged particles separately. It is seen that the efficiency is low for particles with very low transverse momentum. These particles don't reach the TPC, making them harder to track. Since the contaminations are also highest at low momentum, a lower limit of $p_T < 0.2$ GeV/c was chosen. Figure 4.2 shows the single particle correction factor computed according to equation 4.1. The differences between multiplicities are minimal, especially in the region of interest $0.2 < p_T < 2.0$ GeV/c.

4.3 Multiplicity

The study presented in this document focuses on the dependence of the balance function width on the event multiplicity. Events are placed in a multiplicity class using the VZERO detectors V0A and V0C. They cover the ranges $2.8 < \eta < 5.1$ on the A-side and $-3.7 < \eta < -1.7$ on the C-side, respectively. Since these detectors don't provide tracking information, the amplitude of the signal of a cell is proportional to the number of particles that hit that cell and can be used as a proxy for the multiplicity of an event. In the case of Xenon-Xenon collisions, both the V0A and V0C are used. The amplitudes of both detectors are summed and the centrality estimator is referred to as V0M in the analysis. The V0M amplitude for each event is collected in a histogram, which is then divided into percentiles, such that the 0-5% percentile contains the 5 percent of events with the highest V0M amplitude and thus the highest event multiplicity. In this analysis, we compute the balance function for multiplicities between 0-80%. Events in the multiplicity bin 80-100%
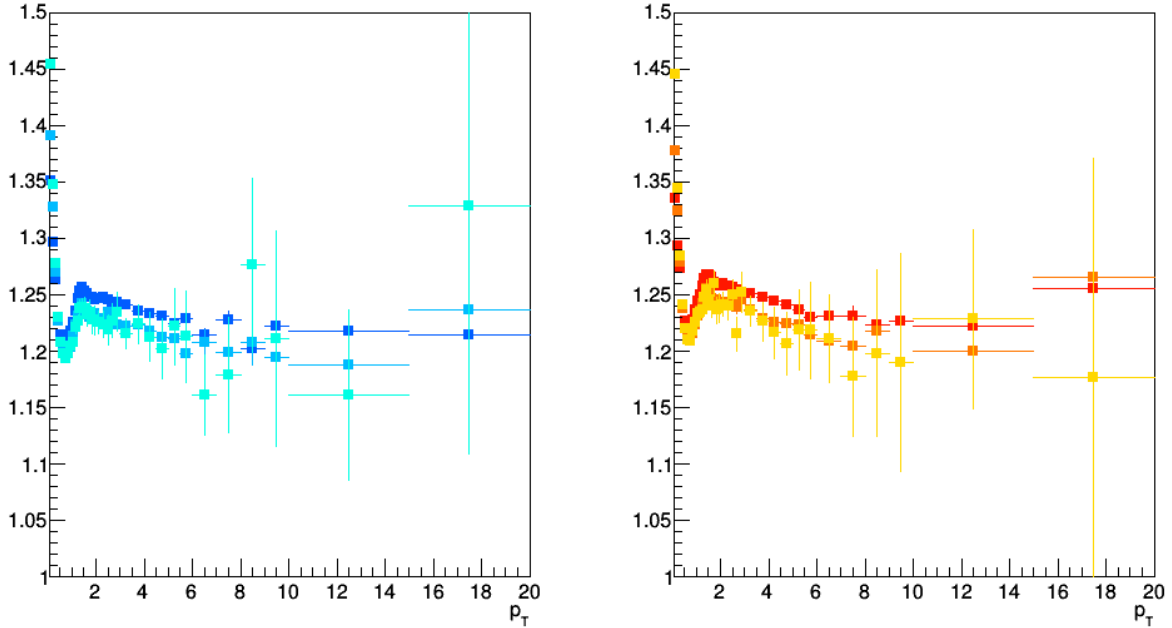
Figure 4.2: The single-particle correction factor, as determined by equation 4.1 for particles with positive (left) and negativ (right) charge. Plotted for the 0-5%, 30-40% and 70-80% multiplicity classes, where darker colours correspond with higher multiplicity.

were not used because of the peculiar behaviour in terms of statistics as well as the significant contribution from diffractive events. Figure 4.3 shows the V0M signal, divided into multiplicity classes. The distribution is also fitted with an NBD-Glauber model with which one can estimate the number of participating and colliding nucleons [29, 30].

It should be noted that in the analyses of the other systems, p-p, Pb-Pb and p-Pb, the V0A signal was used as a proxy for multiplicity. This detector is located in the direction of the Pb-ion in p-Pb collisions and is thus sensitive to its fragmentation [31]. For consistency, the V0A was chosen as the multiplicity estimator for the other two systems. However, this was not possible for the Xe-Xe data. To compare the results for Xe-Xe with the other systems, the multiplicity classes are converted to an average number of charged particles. This was done by counting the number of accepted tracks in each event, over the full $p_T > 0.2$ GeV/c range. The same single-particle correction factors as mentioned in Section 4.2 were used to get a weighted p_T spectrum of the multiplicity of all these tracks, from which the number of reconstructed particles was determined per multiplicity class.
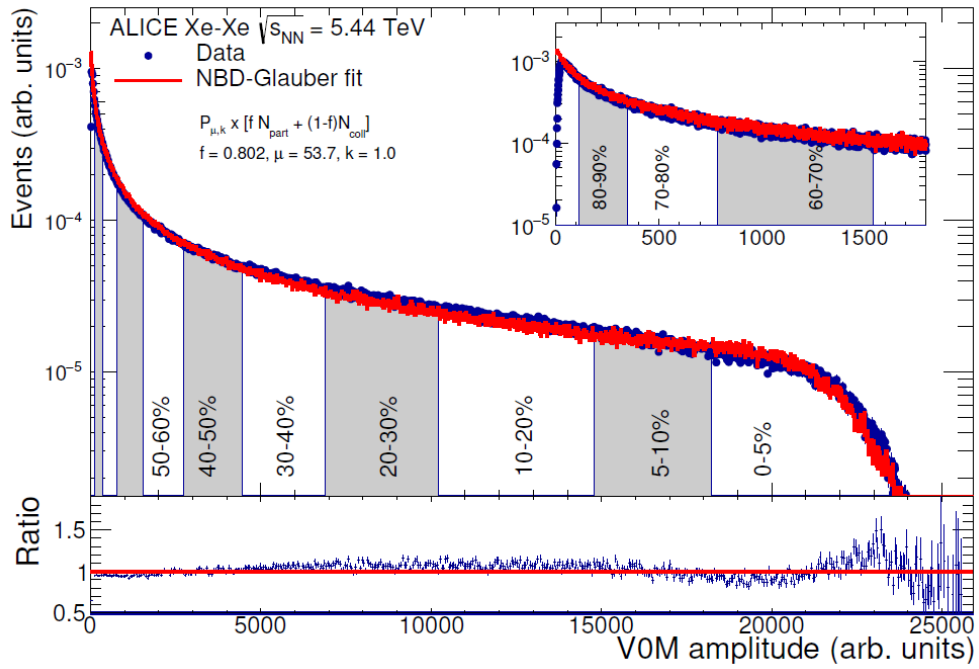
Figure 4.3: Distribution of the sum of amplitudes in the V0 scintillators. The distribution is fitted with the NBD-Glauber model, shown as a line. A few centrality class examples are indicated in the figure. The inset shows a zoom of the most peripheral region. Lower panel: Ratio of the V0M data distribution by the distribution obtained from the NBD fit [30].

Chapter 5

Systematic uncertainties

In the following results of the widths in $\Delta\eta$ and $\Delta\varphi$ as well as the yields, the systematic uncertainty is included. This chapter describes the sources of systematic uncertainty that were investigated and the procedure that was used. For each source of systematic uncertainty that is considered, the associated analysis parameters were varied to give one or more *trials*. To calculate the contribution of each source to the systematic uncertainty, the results of the trials are compared with the default measurement. Only the trials that produce results with significant differences relative to the default ones are taken into account, as described in Section 5.1. An overview of the final values and the maximum relative contributions can be seen in Table 5.1 for the widths in $\Delta\eta$ and in Table 5.2 for the widths in $\Delta\varphi$. It is important to note that all trials were done without corrections and compared to the default results without corrections. There were technical issues with performing a closure test on the corrections, so an estimate is given, as explained below.

5.1 Protocol description

To determine the contribution of each source, the difference between the trials and the default result was calculated. The trial and default results were considered fully correlated, so the statistical uncertainty of the difference was calculated as the square root of the difference of the squared statistical uncertainties of each result. If half or more of the points lies further than one standard deviation (σ) away from zero or if there is a clear systematic trend, i.e. almost all points lie below 0 (even if it is within 1σ) the source was considered to be contributing to the systematic uncertainty. The difference was then fitted and half the fit value was taken as the systematic uncertainty, thus symmetrizing the error. In case of an unclear trend, the uncertainty of this fit decided if a trial was included. If the fit value agrees with zero within 1σ, the trial does not contribute to the systematic uncertainty. The trial with the largest absolute value is taken to contribute to the total systematic uncertainty. All sources are then added in quadrature. This resulted in a relative systematic uncertainty of at most 0.7% and 1.2% for $\sigma_{\Delta\eta}$ and $\sigma_{\Delta\varphi}$, respectively.

As an example of the procedure, Figure 5.1 shows the differences with the default for different track selections, as mentioned in the previous section, filter bits 16 and 768. Note that the horizontal error bars just show the bin size. Both trials show a majority of points more than 1σ away from zero. Therefore a straight line was fitted and half of the fit value is taken. In this case the value for the trial with filter bit 16 is taken to contribute.

Figure 5.2 however, shows the differences with the default for two $\Delta\varphi*$ cuts, where a trend is less clear. In Figure 5.2a there is not a majority of points more than 1σ away from zero and there is not a clear systematic trend. Indeed, a fit gives values -0.0011 ± 0.0013 which is compatible with zero. As a result, this trial did not contribute to the systematic uncertainty. For the other trial, shown in Figure 5.2b, there is also no majority 1σ away, but it is not obvious there is no systematic trend. The fit gives a value of -0.0035 ± 0.0018 agreeing with zero only at 2σ. Therefore half of this value is taken to contribute to the total systematic uncertainty.

The results are summarized in Tables 5.1 and 5.2, for the width in $\Delta\eta$ and $\Delta\varphi$ respectively. The values are used for all multiplicity bins and the percentage of the systematic uncertainty per source is calculated with respect to the smallest value of the width of the default measurement, at 0-1%. Note that even though
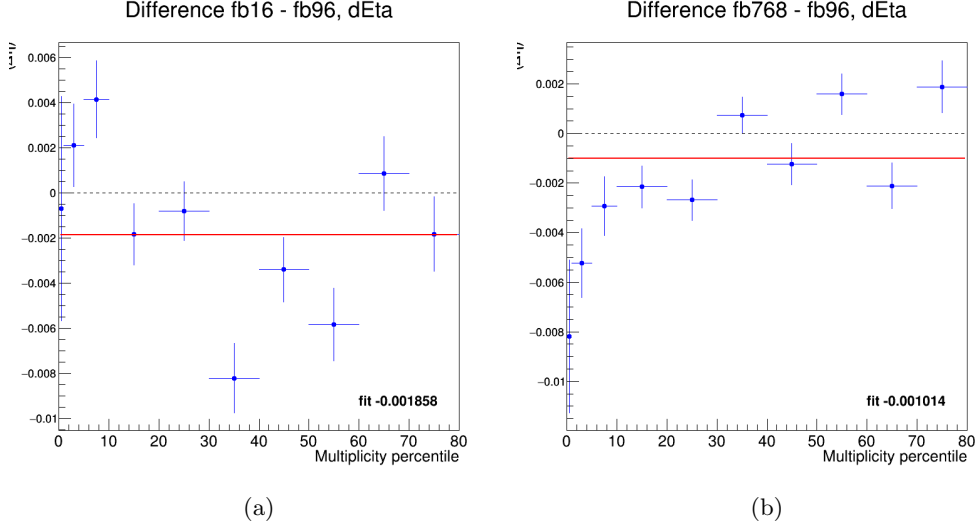
Figure 5.1: Difference between the trials (filter bits 16 and 768, respectively) and the default (filter bit 96) for $\sigma_{\Delta\eta}$, the width of the projection of the balance function in $\Delta\eta$. Both have a majority of points more than 1σ from 0, so this source contributes to the systematic uncertainty.
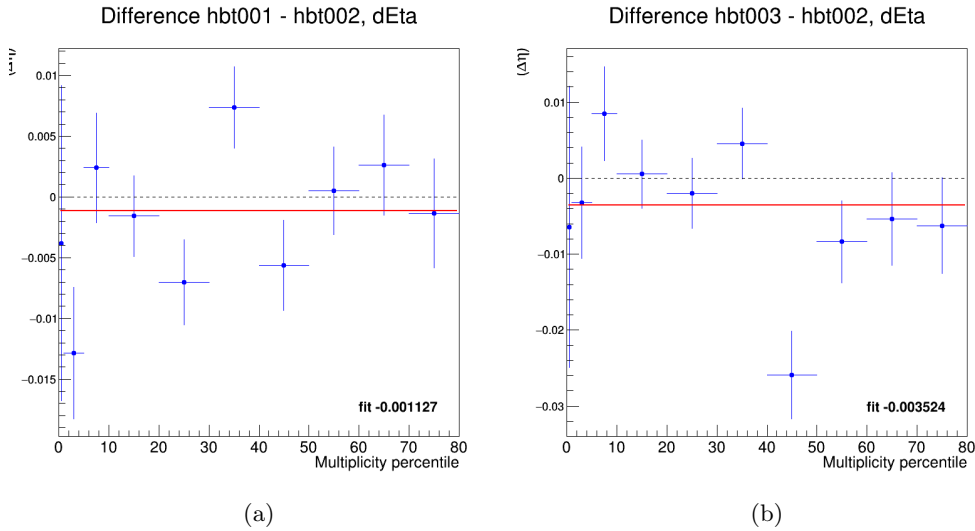

Figure 5.2: Difference between the trials for the $\Delta\varphi*$ cut (0.01 and 0.03 rad, respectively) and the default (0.02 rad) for $\sigma_{\Delta\eta}$, the width of the projection of the balance function in $\Delta\eta$. Both are compatible with 0 and do not contribute to the systematic uncertainty of $\sigma_{\Delta\eta}$.

estimates for the contribution of the closure test and the magnetic field are given in the table, these were not added to the systematic uncertainties in the following plots.

5.2 Sources

Several sources were taken into consideration for the systematic uncertainty, based on the experience from previous research [20]. First of all, the general track selection was varied. The default measurement uses standard cuts (see Section 4.1) on the particle tracks reconstructed by both the ITS and the TPC, while also requiring a cluster in the SDD or SPD layer and tight DCA. Two trials were used. While the first trial uses the same standard cuts, but with a very loose DCA cut and without the additional χ^2 cut on the TPC
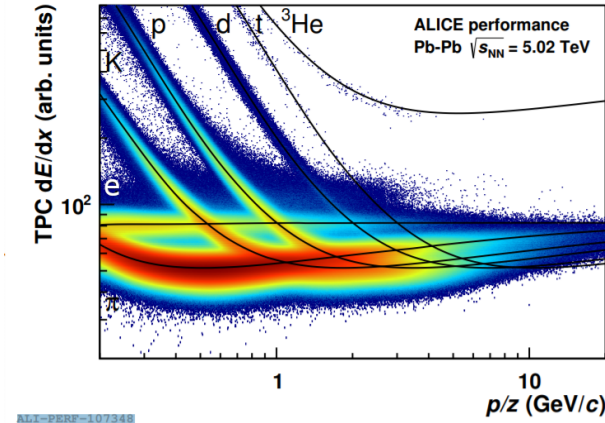
Figure 5.3: Energy loss measured by the TPC as a funciton of rigidity for positive tracks, in Pb-Pb collisions at $\sqrt{s_{NN}} =$5.02 TeV.

fit, the second trial used two complementary sets of track selections. The first of which uses the standard cuts with the golden χ^2 requirement of the TPC fit, as well as the requirement of a hit in the SPD, but with loose DCA cuts. The second set uses tracks that pass the standard cuts but do not leave a signal in the SPD. These variations produced systematic uncertainties of 0.21% and 0.54% for the width in $\Delta\eta$ ($\sigma_{\Delta\eta}$) and $\Delta\varphi$ ($\sigma_{\Delta\varphi}$), respectively.

Additional track selection parameters were changed in trials. The requirement on the closest distance of tracks of a pair in the TPC was varied from $\Delta\varphi^* = 0.02$ rad to $\Delta\varphi^* = 0.01$ and $\Delta\varphi* = 0.03$. This resulted in a maximum relative contribution of 0.4% to the systematic uncertainty of $\sigma_{\Delta\eta}$, while it did not contribute for $\sigma_{\Delta\varphi}$. Further requirements on the TPC reconstruction were varied as well. The minimum number of TPC clusters was varied from 70 to 100, which gave a contribution of max. 0.48% to $\sigma_{\Delta\eta}$, but none to $\sigma_{\Delta\varphi}$. The maximum χ^2 per cluster in the TPC was varied from $\chi^2 = 4$ to $\chi^2 = 3$ in the trial, but this did not contribute to the systematic uncertainty of the widths.

The uncertainty introduced by the electron rejection criterion was also studied. Electrons need to be excluded since this analysis only concerns charged hadrons and electrons make up a large background due to pair production. At low momentum, the electron identification is mainly based on the measurement of the energy loss in the TPC. A cut is applied using a region of $n\sigma$ around the Bethe-Bloch parametrization of the energy loss dE/dx. As seen in Figure 5.3, the electron rejection region has an effect on the hadrons that get reconstructed correctly. The rejection region was varied from 3σ to 5σ in the trial. This resulted in a maximum relative contribution of 0.053% to the systematic uncertainty of $\sigma_{\Delta\varphi}$. It did not contribute to the systematic uncertainty of $\sigma_{\Delta\eta}$.

The position of the primary vertex on the beam axis is indicated by V_z. In the default measurement, the region $V_z \in [-10, 10]$ was used. Trials used smaller regions with $V_z \in [-7, 7]$, $V_z \in [-5, 5]$ and $V_z \in [-3, 3]$. The contribution of this source to the systematic uncertainty is 0.064% and 0.27% for $\sigma_{\Delta\eta}$ and $\sigma_{\Delta\varphi}$, respectively.

Although pile-up is not expected to be a problem in the Xe-Xe data as much as it is in p-p collisions, the effect is analyzed by changing the selection algorithm used to identify the primary vertex. Tracks from pile-up events can be excluded since they point to the wrong vertex. While the default algorithm uses tracks (reconstructed by the ITS and TPC) to identify the primary vertex, the algorithm used in the trial uses only clusters in the SPD. This did not contribute to the systematic uncertainty in $\sigma_{\Delta\varphi}$, following the procedure described above. For $\sigma_{\Delta\eta}$ however, it contributed a maximum relative uncertainty of 0.3%.

Finally, to check whether the corrections are applied correctly, a closure test should be done where the analysis is performed on Monte Carlo generated production data and on the simulated reconstructed data. If the corrections are applied to the reconstructed data correctly, the analysis should give exactly the same result as the analysis on the generated particles. For this research on Xe-Xe collisions some technical problems prevented us from performing it. As an estimate, the contribution to the systematic uncertainty

is taken from a previous study [20]. This is done since the machinery did not change and has been tested in all previous instances. There was no reason thus to suspect that it would not work also in the Xe-Xe case. A range is given, 0.4 - 1.1%, using the values from p-p and Pb-Pb, since the system size is comparable to Pb-Pb, but the way of applying the corrections was done the same as in p-p.

It should also be mentioned that the magnetic field was the main source of systematic uncertainty in the Pb-Pb analysis. Unfortunately there is no data available for Xe-Xe collisions with different magnetic field polarity. For the sake of comparison, the maximum contribution of the magnetic field to Pb-Pb, 1.5% is also indicated.

Table 5.1: Systematic uncertainties for $\sigma_{\Delta\eta}$, both the absolute value and relative to the central value at 0-1%. *Estimates from p-p and Pb-Pb analyses.

Source	value	max %
Filter bit	0.00093	0.21
$\Delta\varphi*$	0.00176	0.40
TPC clusters	0.0021	0.48
Pile-up	0.00132	0.30
V_z	0.00028	0.064
Closure test*		0.4 - 1.1
Magnetic field*		1.5

Table 5.2: Systematic uncertainties for $\sigma_{\Delta\varphi}$, both the absolute value and relative to the central value at 0-1%. *Estimates from p-p and Pb-Pb analyses.

Source	value (rad)	max %
Filter bit	0.0032	0.54
Electron rejection cut	0.0063	1.1
V_z	0.0016	0.27
Closure test*		0.4 - 1.1
Magnetic field*		1.5

Chapter 6

Results

The Xe-Xe sample collected by ALICE in 2017 was analysed using the selection criteria described in Chapter 4. The main results for the charge-dependent balance functions will be discussed in the following sections. The balance function is presented in its two dimensional form and subsequently the width and yield are extracted from projections. The widths and yields are shown with systematic uncertainties, which are described in Chapter 5. Finally, these widths will be compared to model expectations and to results of other collision systems to be able to draw conclusions about the origin of collective effects in high-energy collisions.

6.1 Two dimensional balance functions

Figure 6.1 shows the balance functions for three different multiplicity classes, while the remaining plots for the other multiplicity classes are shown in Appendix A, Figure A1. In particular the following intervals are shown: 5-10% (high multiplicity, more central events), 30-40% (medium multiplicity, mid-central events) and 60-70% (low multiplicity, peripheral events). Compared to the correlation function shown in Figure 3.2, the balance function looks different. The away-side ridge at $\Delta\varphi = \pi$ and the near-side ridge at $\Delta\varphi = 0$ have now disappeared. The away-side ridge is due to jets and reflects correlations between two particles in back-to-back topologies, while the near-side ridge is interpreted as a sign of anisotropic flow (see Section 1.1). However, these are present in both the like-sign and the unlike-sign correlation functions and when constructing the balance function by taking their charge-dependent differences they cancel out. What remains is a central peak around $(\Delta\eta, \Delta\varphi) = (0, 0)$. It can be seen that this peak changes shape between the multiplicity classes. At high multiplicity, on the left, the peak is narrower than at the lower multiplicities as observed in the middle and on the right. This result was expected since it was also observed in Pb-Pb collisions and recently in smaller collision systems. The current explanation for this narrowing in heavy-ion collisions is mainly the explosive expansion of the quark-gluon plasma. As mentioned in Chapter 1, the QGP created in a heavy-ion collision behaves like a fluid and expands, introducing collective motion to the partons in it: radial and anisotropic flow. This translates to correlations between the created particles, similarly to how a kinematic boost works. The balance function is a probe for the amount of radial flow in the system by measuring the correlation between balancing charges. The idea is that balancing charges are created at the same point in space and time and their correlation is a sign of the boost applied to the center-of-mass of the interaction of their creation. A larger boost will result in the pair having a smaller angular separation. Overall, this results in a narrower balance function. The boost depends on the expansion velocity of the system, which is expected to depend on the pressure gradient of the QGP [4, 8]. As mentioned in Chapter 1, the size and pressure gradient depend on the centrality of the collision. This leads to the conclusion that balancing pairs will have smaller angular separation, i.e. the balance function will be narrower, with increasing multiplicity. This is indeed what can be observed in Figure 6.1. In the orientation of the plot the peak is seen to extend to a smaller region in $\Delta\eta$ for high multiplicity, 0-5%, compared to low multiplicity, 60-70%.

To further inspect this narrowing, Section 6.2 will show the projections in both the $\Delta\eta$ and $\Delta\varphi$ direction and the widths of the peaks will be discussed in Section 6.3. These results are shown with systematic uncertainties, obtained as described in Chapter 5.
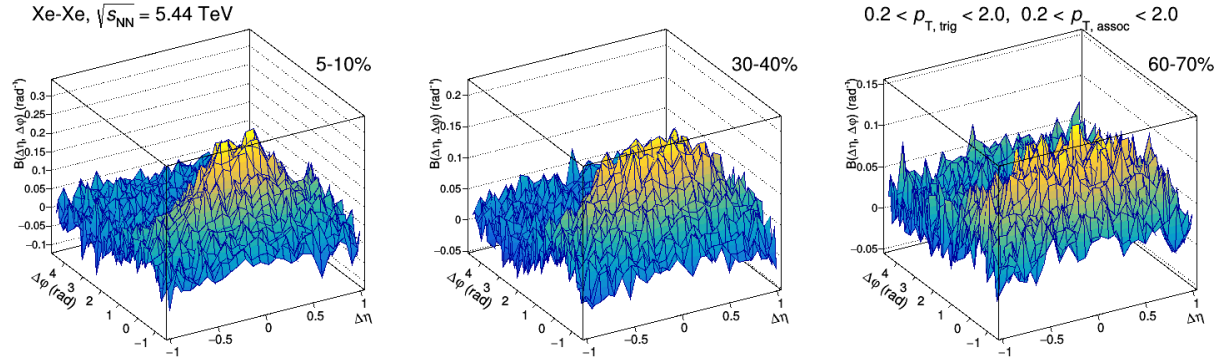
Figure 6.1: The balance functions of charged particles for multiplicity classes 5-10%, 30-40% and 50-60%.

Before presenting the remaining results, it is important to note that the multiplicity percentile classes used in this analysis lie between 0-80%, divided in bins of 10%, except for the highest multiplicity classes (below 10%). These were divided in three classes: 0-1%, 1-5% and 5-10%[1]. This was done to study the effect of the shape of the xenon nucleus on the balance function. Previous studies have shown that the slight prolate deformation of the xenon nucleus [32] results in a different signature in observables that probe the initial state of anisotropy. The eccentricity ϵ_2 of the system translates to an elliptic momentum distribution, reflected in the v_2 distribution, as mentioned in the introduction. The elliptic flow (v_2) is predicted to be 25% larger in Xe-Xe than in Pb-Pb at high multiplicity (0-5%) and 10% smaller for lower multiplicity (above 30%) [33].

The effect is not expected to show in the balance function itself, since in this version of the analysis the correlations are integrated over the entire azimuth. Any preferred direction in the out-of-plane direction will not be probed, since only the angular separation between pairs is used. Moreover, like any anisotropic flow effect it is, in principle, charge independent. This means it cancels out when subtracting the like-sign correlations in Equation 3.1. Still, this was considered a good reason to at least investigate the high multiplicity region more closely.

6.2 Projections in $\Delta\eta$ and $\Delta\varphi$

Figure 6.2a shows the projection of the balance function in pseudo-rapidity, using only the near side ($-\pi/2 < \Delta\varphi < \pi/2$) of the distribution. Figure 6.2b shows the projection of the balance function in the azimuthal angle. Both are shown for three different multiplicity classes: 5-10%, 30-40% and 60-70%. All multiplicity classes are shown in Figure A3. It is clearly seen that the shape changes with increasing multiplicity. A dip in the balance function at $(\Delta\eta, \Delta\varphi) = (0,0)$ is now easily seen. This depletion, that becomes more pronounced for lower multiplicities was also observed in other systems, where it was more pronounced for the smaller systems, i.e. p-p and p-Pb. The proposed mechanisms that could create such a structure are charge-dependent short-range correlations, such as Coulomb attraction and repulsion or quantum-statistics correlations [20, 34]. In the study of p-p collisions this structure was seen to disappear when increasing Δp_T from 0 to 0.2 GeV/c. Since the short range correlations originating from quantum statistics are expected to have $\Delta p_T < 0.1$ GeV/c, this is consistent with the proposed mechanisms [21]. Additionally, this study in p-p showed that another possible mechanism that could contribute to this depletion is the decay of resonances. Balance functions of pions were simulated using PYTHIA8, selecting only resonance decays, specifically ω and ρ^0 mesons. Both show a depletion at $(\Delta\eta, \Delta\varphi) = (0,0)$ caused by the decay kinematics that favours $\pi^+ + \pi^-$ production in opposite directions and larger separation angles, respectively [21].

---

[1]It should be noted that the corrections were determined for 0-5%, 5-10%, 10-20% etc. The differences between the corrections were small enough to justify this simplification.
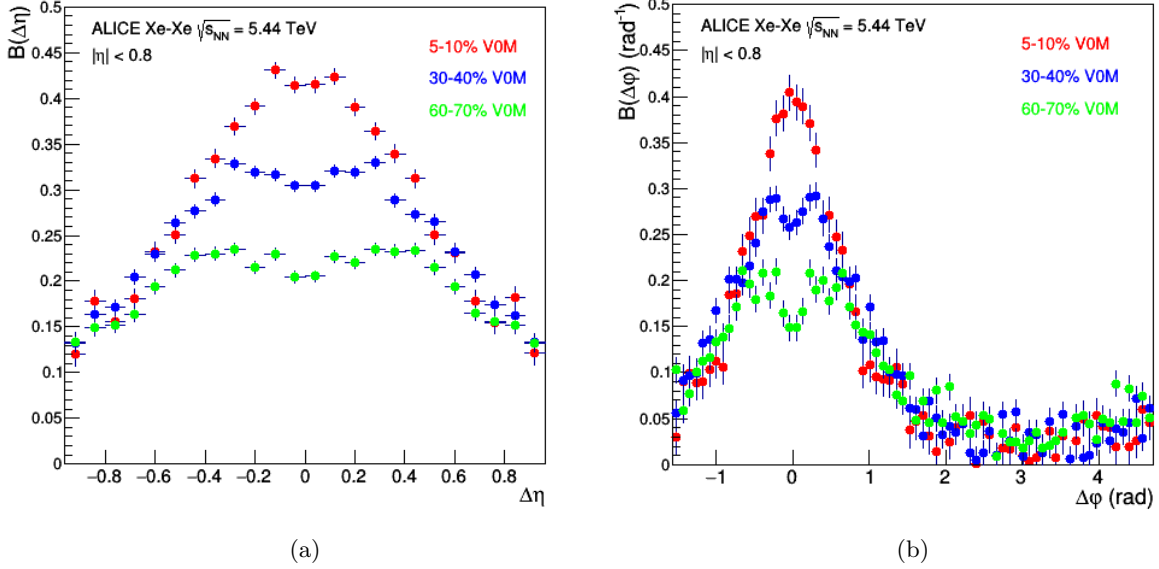
(a)	(b)

Figure 6.2: The projection of the balance functions on $\Delta\eta$ for the near-side ($-\pi/2 < \Delta\varphi < \pi/2$) (a) and on $\Delta\phi$, for multiplicity classes 5-10% (red), 30-40% (blue) and 60-70% (green).

6.3   Width of the balance function

To evaluate the behaviour of the balance function, the widths of the projections shown in the previous section were taken. Figure 6.3 shows the widths in $\Delta\eta$ and $\Delta\phi$ for all multiplicity classes. The statistical and systematic uncertainties are indicated by the blue bars and red brackets, respectively. As mentioned in Chapter 5, the systematic uncertainties are the same for every multiplicity class and do not include the closure test. The statistical error is seen to be larger for the 0-1% multiplicity class, where the number of analyzed events is lower. From these two plots it is easily seen that the width of the balance function in both directions significantly decreases when moving to higher multiplicity. It should be noted that previous studies have verified that the depletion at $(\Delta\eta, \Delta\varphi) = (0,0)$ is not the source for the broadening of the balance function. Removing it by changing the p_T range as discussed above, keeps the trend intact [20, 21].

The most plausible physical mechanism to produce this narrowing of the balance function with increasing multiplicity is radial flow. After all, the radial flow that influences the correlation between balancing pairs depends on the size and pressure gradient of the system, as explained in Chapter 1. This in turn is determined by the centrality of the collision. The number of nucleons participating in the collision and thus the multiplicity depends on this centrality. Moreover, models without such collective expansion fail to produce the observed narrowing, as demonstrated by the HIJING model in Section 6.5.

A deviation from the trend can be seen at 1-5% in Figure 6.3a. It was a recurring feature in the analysis when including corrections and should be investigated. A smaller fluctuation can be seen at 30-40% in the $\Delta\eta$ width in Figure 6.3b, but this is within uncertainties. Regarding the discussion in Section 6.1, this analysis shows no conclusive evidence of effects of the prolate deformation of the xenon nucleus.

6.4   Yields

Figure 6.4 shows the yields of the balance function for three regions, the away-side ($\pi/2 < \Delta\varphi < 3\pi/2$), near-side ($-\pi/2 < \Delta\varphi < \pi/2$) and the total ($\Delta\eta, \Delta\phi$) which is the sum of the other two. This total yield corresponds to the integrated balance function mentioned in Equation 3.5. Therefore the maximum value is expected to be 1. Instead, the total yield lies between 0.6 and 0.8. This means that 60-80% of the correlated pairs have been reconstructed in the acceptance range $|\eta| < 0.8$. It is seen that around 90% of this correlation is measured in the near-side region. Moreover, a decrease in the total yield is seen for lower multiplicity.
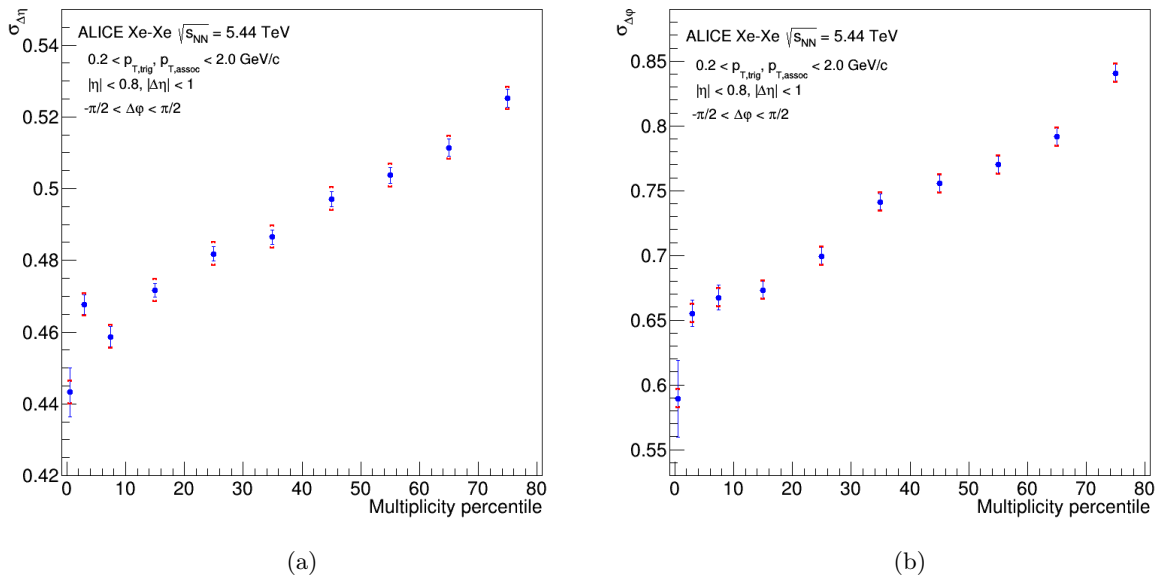
Figure 6.3: Widths of the balance function projections in $\Delta\eta$ (on the near-side) and in $\Delta\phi$, for all multiplicity classes. Systematic uncertainties are indicated in red.

This makes sense considering the broadening of the balance function (see Figure 6.1), leading to pairs falling outside the detector acceptance range. The two most central bins show the recurring fluctuation again, which is not fully understood yet. Nevertheless, the trend is clear for 5-80%.

6.5 Model expectations

The balance function widths were compared with results of the analysis performed on simulated data from HIJING (Heavy-Ion Jet Interaction Generator) [27]. This Monte Carlo model combines a perturbative QCD inspired model for multiple (mini-)jet production with the Lund string model [35] for jet hadronization to simulate the particle generation in Xe-Xe collisions. It describes a heavy-ion collision as multiple nucleon-nucleon collisions, where the concept of jets from hard parton scattering is well established. At low transverse momentum these jets are referred to as minijets. These have energies too low to be resolved experimentally ($E_t < 5$ GeV), but they could lead to a wide variety of correlations. Since these minijets are estimated to produce a majority of the total transverse energy [36], they make up a significant background to the expected QGP signatures. It is therefore important to investigate how the balance function behaves for this model.

The analysis aimed to use the same multiplicity classes for the HIJING generated particles as for the data However, to limit the computation time, the multiplicity classes were limited to: 0-5%, 5-20%, 20-40%, 40-60% and 60-100%. These classes were defined by dividing the generated N_{ch} distribution into quantiles. After running the balance function analysis on these multiplicity classes, the average multiplicity for each class was used in the results. Note that this model does not include the detector response. The particle selections were the same as used on the ALICE data, e.g. $0.2 < p_T < 2.0$ GeV/c, $|\eta| < 0.8$ and $-\frac{\pi}{2} < \varphi < \frac{\pi}{2}$.

Figures 6.5a and 6.5b show the widths of the balance function, this time plotted with respect to multiplicity. The multiplicity of the data was determined using the method described in Section 4.3. Figure 6.5 shows that the model is not able to reproduce the results from the data. Though the values of the widths are comparable at low multiplicities, especially for $\sigma_{\Delta\eta}$, it fails to show the same narrowing of the balance function. It does show a visible decline when moving to higher multiplicities, but not to the same degree as the data. This also agrees with a previous study on Pb-Pb collisions, where HIJING doesn't show any narrowing of the balance function widths [20]. This allows to conclude that the narrowing of the balance function is due to a process that is not included in the model. Since the HIJING model does not incorpo-
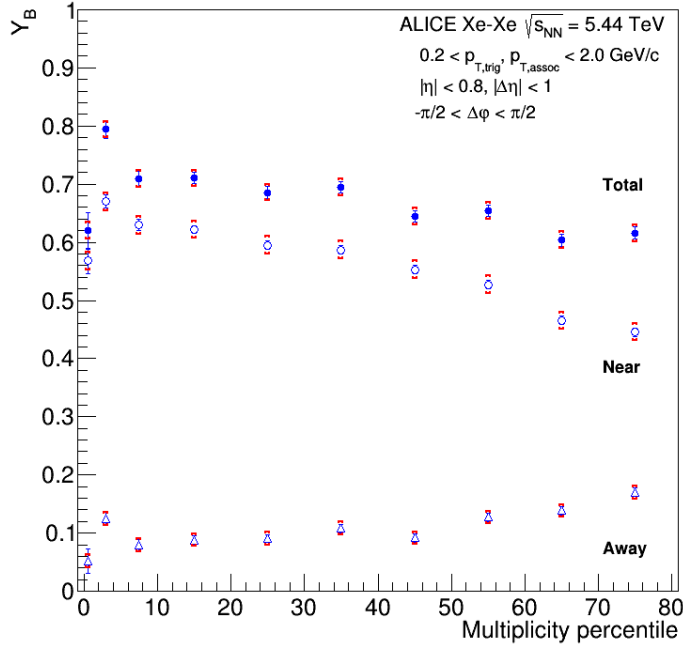
Figure 6.4: The yield of the balance function as a function of multiplicity class, for the away region, near region and in total. Systematic uncertainties are indicated in red.

rate hydrodynamics or other collective effects, this supports the idea of the narrowing originating from the explosive expansion of the medium created in heavy-ion collisions.

6.6 Comparing collision systems

Figure 6.6 shows the widths of the balance function projections in $\Delta\eta$ of this analysis together with previous results from studies using proton-proton, proton-lead [21] and results from lead-lead collisions[2] at $\sqrt{s_{NN}} = 5.02$ TeV . It should be noted that the analysis on Xe-Xe uses data collected in the full $\eta \in [-0.8, 0.8]$ range, while the other studies only used $\eta \in [-0.5, 0.5]$. Also, while this analysis used a $\Delta\eta$ range of $[-0.96, 0.96]$ when calculating the projection, in accordance with the p-p and p-Pb analyses, the Pb-Pb analysis uses a different range, $[-1.36, 1.36]$. This logically results in higher values of the widths. To visually compare the results more easily, the Pb-Pb points have been scaled down with a scaling factor of 0.96/1.36. No meaning should be taken from these scaled absolute values of the Pb-Pb points or the absolute difference between Pb-Pb and Xe-Xe. That being said, it can be seen that the systems align quite well. Together they show a clear trend of narrowing of the balance function peak with increasing multiplicity. The slope of the Xe-Xe results is similar to the Pb-Pb results and the increase in slope at higher multiplicity is also seen. At lower multiplicity, the results approach those of the smaller systems.

Compared to p-p and p-Pb, the statistical uncertainties in Xe-Xe are larger. This is to be expected since the Xe-Xe data set is limited to around 1.8×10^6 analyzed events, whereas the p-p results used 6.5×10^8 analyzed events. The analysis in Pb-Pb was performed on low interaction rate data only.

Figure 6.7 shows the comparison between systems for the width of the balance function in the $\Delta\varphi$ projection. Since no scaling for Pb-Pb was necessary in this case, it shows the similarities even better than the results for $\sigma_{\Delta\eta}$. A small difference is seen between the p-Pb results and the results for the two

---

[2]These results are preliminary, using methods that match the small systems and this analysis. Previous results in Pb-Pb are shown in [37].
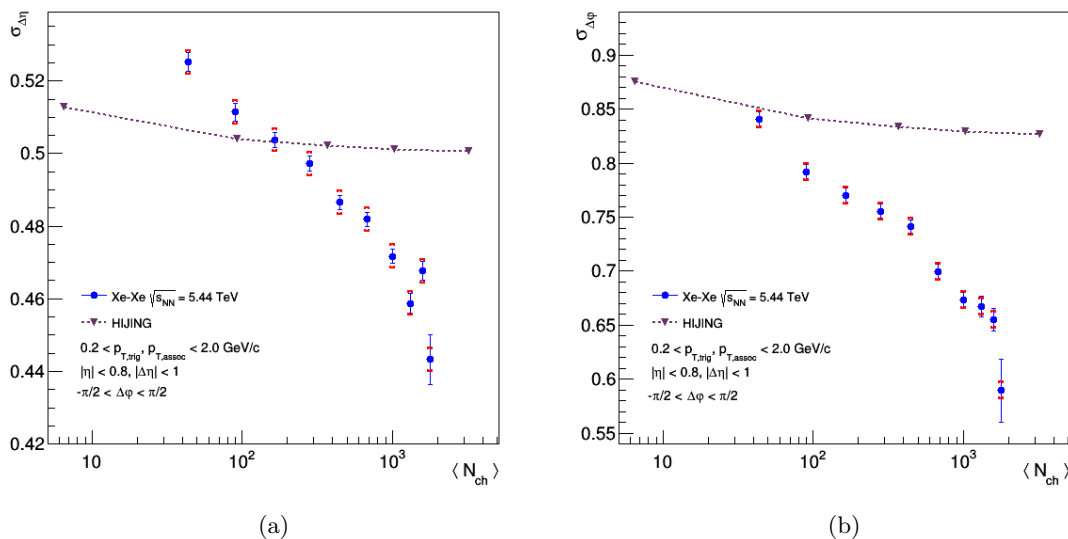
Figure 6.5: Widths of the balance function in $\Delta\eta$ (a) and $\Delta\varphi$ (b) with respect to multiplicity (red systematics) compared to results from HIJING. Statistical uncertainties in the HIJING results are too small to be visible.

bigger systems. This was also observed in previous studies [20], and has been interpreted as a still unknown difference in the mechanisms between the systems.

However, both plots show a smooth evolution of the balance function width with increasing multiplicity. This allows to conclude that the collective effects depend on the multiplicity. This smooth transition as a function of multiplicity could point to a common physics origin, e.g. the creation of a QGP that expands explosively in all collision systems. After all, as mentioned in Chapter 1 and discussed in Section 6.1, the QGP is described as an expanding perfect fluid, giving rise to a radial flow that boosts the particles and causes correlations of balancing charged particles at smaller angles. This results in a narrowing of the balance function.

It is tempting to conclude that a small quark-gluon plasma is formed in p-p and p-Pb collision, by analogy with the larger systems. The presence of the QGP in Pb-Pb systems is well supported by observables like the momentum distributions v_n and jet quenching, see Section 1.1. However, still a small gap is observed between the small systems and the large systems. Moreover, the slope of both Xe-Xe and Pb-Pb, while similar at low multiplicity, is seen to increase at high multiplicity. This implies a different origin of the collective motion in the central heavy-ion collisions compared to the small systems. This raises the question whether this mechanism that is the cause of "radial-flow-like" behaviour in small systems also contributes to the collective effects in peripheral heavy-ion collisions. Section 7.1 will discuss the next steps in the study of the small systems using the Xe-Xe data.

Section 3 mentioned that the balance function is a sensitive probe to the creation time of quarks in a heavy-ion collision. The later a balancing pair is created, the further they can separate in the collective expansion of the system, resulting in a wider balance function. According to [17], the overall width of the balance function (in $\Delta\eta$) is a combination of the thermal spread and the effect of diffusion on both particles, such that:

$$\sigma_{total}^2 = \sigma_{therm}^2 + \sigma_\eta^2. \tag{6.1}$$

The thermal spread is proportional to $\sqrt{T/m}$, resulting in heavier particles having narrower balance functions. However, if the production occurs early, the diffusion term is large and the balance function width will be larger. Since the balance function widths of the different systems overlap nicely, this implies that the time of creation is the same in all systems. This implies similar conditions of the system before hadronization. Though, without an accurate model to compare to there is no way to actually determine the creation time. It was suggested at the time to compare with p-p collisions at the same $\sqrt{s_{NN}}$, where hadronization was assumed to be nearly instantaneous [17]. Indeed the aim of the measurements on azimuthal correlations in
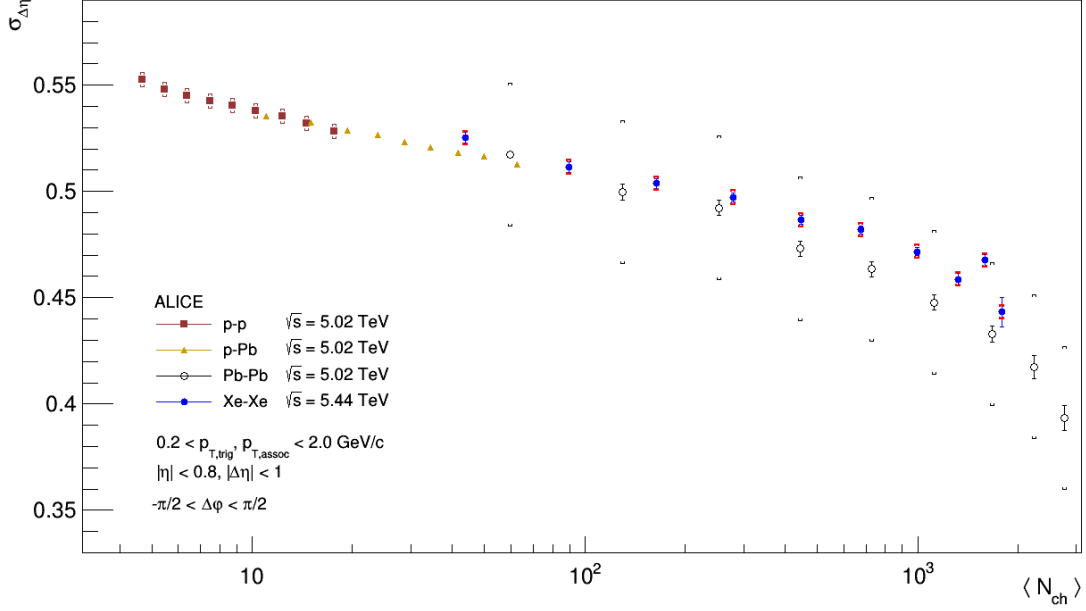
Figure 6.6: Comparison of the widths of the balance function projection in $\Delta\eta$ ($\sigma_{\Delta\eta}$) between systems p-p, p-Pb, Pb-Pb ($\sqrt{s_{NN}} = 5.02$ TeV) and Xe-Xe ($\sqrt{s_{NN}} = 5.44$ TeV). Where the Pb-Pb results are scaled down by an arbitrary factor, see text.

small systems was to provide reference data for the heavy-ion collisions. The unexpected signals of collective flow that were observed in these small systems made this more complicated. However, as discussed in Section 7.1, studies of the balance function for different species, e.g. pions, kaons and protons, should give more insight into the relative creation time of the different quark flavours. In particular, if the quark pairs are created at a late stage, the thermal term in Equation 6.1 would be dominant and the differences between particle species would be more evident in the resulting balance function widths.
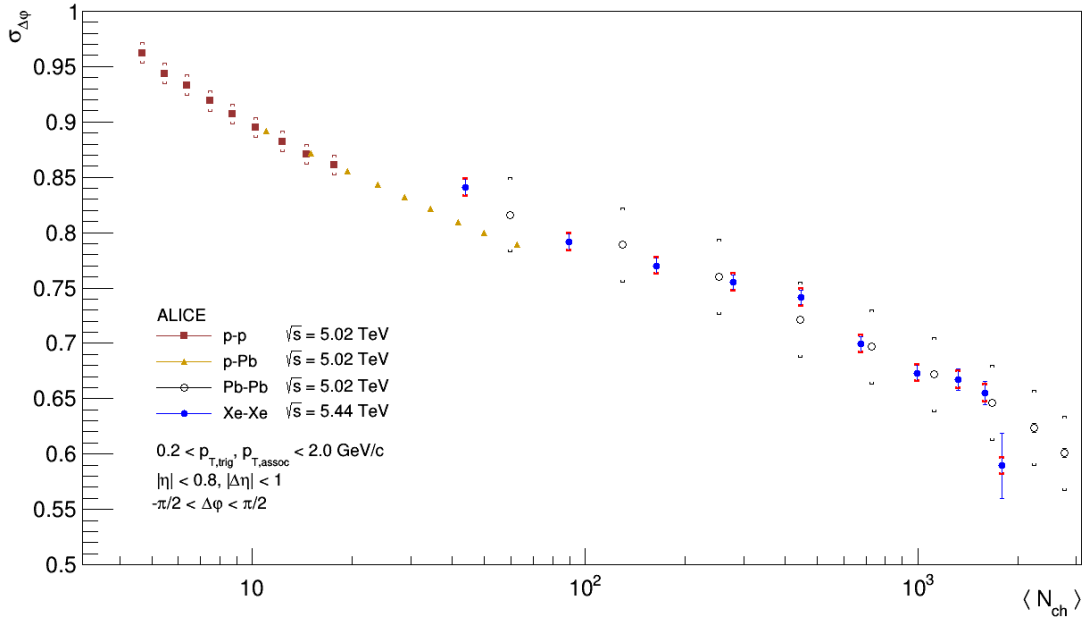
Figure 6.7: Comparison of the widths of the balance function projection in $\Delta\varphi$ ($\sigma_{\Delta\varphi}$) between systems p-p, p-Pb, Pb-Pb ($\sqrt{s_{NN}} = 5.02$ TeV) and Xe-Xe ($\sqrt{s_{NN}} = 5.44$ TeV). Where the Pb-Pb results are scaled down by an arbitrary factor, see text.

Chapter 7

Conclusion

In heavy-ion collisions, a medium called the quark-gluon plasma (QGP) is formed. Its expansion is well described by hydrodynamics. Many properties of this medium can be studied using indirect methods, e.g. jet quenching, flow coefficients (v_n) and two-particle correlations. Recently these studies have been applied to small collision systems, i.e. proton-proton and proton-lead collisions. Although no QGP was initially expected to form in these collisions, similar features were observed that were thought to be a sign of the expansion of the hot, dense medium. This has lead to additional research in these small collision systems. Specifically, the balance function was studied, which quantifies the correlation in pseudo-rapidity (η) and azimuthal angle (φ) between oppositely-charged particle pairs. The balance function is a probe of radial flow, as well as the creation time of quarks in the system. Surprisingly, results in p-p, p-Pb and Pb-Pb show similar results, where the balance function narrows with increasing event multiplicity.

The study presented in this document has measured for the first time the balance function of unidentified charged particles for Xe-Xe collisions at $\sqrt{s_{NN}} = 5.44$ TeV. Compared to the other collision systems, it is most similar to Pb-Pb (A=208), with A=129. The balance function was constructed for different multiplicity percentiles between 0-80%. The 0-1% class contains the events with the highest multiplicity and corresponds to the most central events. To compare with model expectations and other systems, these percentiles were converted to average multiplicities in terms of $\langle N_{ch} \rangle$. The results show that the balance function narrows significantly when the multiplicity increases. This is in agreement with the results in the larger system Pb-Pb. The observed narrowing is shown to be larger than predicted by the HIJING model which does not include any collective expansion. Therefore the results support the hypothesis of an expanding quark-gluon plasma that produces correlations between balancing charges as they experience a boost from radial flow.

A comparison with smaller systems p-p and p-Pb and the larger system Pb-Pb shows that the narrowing of the balance function is consistent over multiplicity. This suggests the collective effects are of a similar nature in all systems. However, there are small differences. Together with unexpected results for identified particles in the small systems and the absence of jet quenching in small systems, this suggests the existence of additional mechanisms could play an important role in small collision systems. Further research is needed, as will be described in the next section.

The balance function is also described as a probe for the creation time of quarks. The results presented in this thesis cannot be used to draw conclusions on this subject, since this would require an accurate model in which the creation time can be varied. However, the Xe-Xe data was proved to be useful in the investigation of the balance function and the next section will describe how to continue.

7.1 Outlook

First of all, the feature that causes the fluctuation in the most central bins should be investigated. As mentioned, it arises when corrections are applied. However, no pattern was obvious when altering the bin sizes, swapping the corrections or using different V_z. Time did not allow to investigate this further in this analysis. It is possibly a bug in the code, but it is best to be understood before moving on.

Secondly, other model expectations could be compared to Xe-Xe collision. Potential models are the EPOS LHC model [38], which incorporates collective effects through a flow parametrisation and the hybrid

model iEBE-VISHNU. Both have shown to reproduce the shape of the charged-particle multiplicity density [39]. The AMPT model applies a hydrodynamical evolution to an initial state produced by HIJING. Though this sounds promising, it has not been able to reproduce the narrowing of the balance function in Pb-Pb or p-p [20], so it is not expected to do so in Xe-Xe. It could be checked nevertheless.

Finally, since previous studies have shown that heavier particles are more sensitive to the collective boost from radial flow, due to momentum dependence, future studies of the Xe-Xe data should focus on identified particles. The balance function for identified particles, i.e. for pions, kaons and protons, has been measured for p-p and p-Pb [21] and surprisingly found that protons show a less distinct narrowing of the balance function width, despite being heavier. This suggests that an effect other than radial flow is responsible for the multiplicity-dependent narrowing in small systems. If the same lack of multiplicity dependence is found for protons in Xe-Xe collisions, this would be a very striking result. Furthermore, studying the balance function of different species might lead to other relevant discoveries, as is the case for the pion resonances mentioned in Section 6.2, which could explain the depletion observed on the near side in all systems. Moreover, the balance function for identified particles could provide important insight in what is referred to as the QGP chemistry: the evolution of parton creation and the way quarks of different flavours balance [21, 40]. As mentioned before, if quark pairs are created at a later stage, the balance function width will be smaller, since the pairs have less time to diffuse to larger separation. A difference in creation time between quark flavours will therefore be reflected in differences between the balance function widths of different hadron species, e.g. baryons, strange hadrons or pions. These studies of the balance function of identified hadrons are also yet to be done on Pb-Pb collisions at $\sqrt{s_{NN}} = 5.02$ TeV. Clearly, the balance function still has a lot of potential.

Bibliography

[1] Szabolcs Borsányi et al. "The QCD equation of state with dynamical quarks". In: *Journal of High Energy Physics* 2010.11 (Nov. 2010). ISSN: 1029-8479. DOI: 10.1007/jhep11(2010)077. URL: http://dx.doi.org/10.1007/JHEP11(2010)077.

[2] J. C. Collins and M. J. Perry. "Superdense Matter: Neutrons or Asymptotically Free Quarks?" In: *Phys. Rev. Lett.* 34 (21 May 1975), pp. 1353–1356. DOI: 10.1103/PhysRevLett.34.1353. URL: https://link.aps.org/doi/10.1103/PhysRevLett.34.1353.

[3] D. Boyanovsky, H.J. de Vega, and D.J. Schwarz. "Phase Transitions in the Early and Present Universe". In: *Annual Review of Nuclear and Particle Science* 56.1 (Nov. 2006), pp. 441–500. ISSN: 1545-4134. DOI: 10.1146/annurev.nucl.56.080805.140539. URL: http://dx.doi.org/10.1146/annurev.nucl.56.080805.140539.

[4] Ulrich Heinz and Raimond Snellings. "Collective flow and viscosity in relativistic heavy-ion collisions". In: *Annual Review of Nuclear and Particle Science* 63 (2013), pp. 123–151.

[5] Mateusz Ploskon. *Heavy-ion collisions - hot QCD in a lab.* 2018. arXiv: 1808.01411 [hep-ex].

[6] B. Abelev et al. "Centrality dependence of π, K, and p production in Pb-Pb collisions at sNN=2.76 TeV". In: *Physical Review C* 88.4 (Oct. 2013). ISSN: 1089-490X. DOI: 10.1103/physrevc.88.044910. URL: http://dx.doi.org/10.1103/PhysRevC.88.044910.

[7] Jean-Yves Ollitrault. "Anisotropy as a signature of transverse collective flow". In: *Phys. Rev. D* 46 (1 July 1992), pp. 229–245. DOI: 10.1103/PhysRevD.46.229. URL: https://link.aps.org/doi/10.1103/PhysRevD.46.229.

[8] Huichao Song, You Zhou, and Katarina Gajdosova. "Collective flow and hydrodynamics in large and small systems at the LHC". In: *Nucl. Sci. Tech.* 28.7 (2017), p. 99. DOI: 10.1007/s41365-017-0245-4. arXiv: 1703.00670 [nucl-th].

[9] S. Acharya et al. "Anisotropic flow in Xe–Xe collisions at $\sqrt{s_{NN}}$ = 5.44 TeV". In: *Physics Letters B* 784 (Sept. 2018), pp. 82–95. ISSN: 0370-2693. DOI: 10.1016/j.physletb.2018.06.059. URL: http://dx.doi.org/10.1016/j.physletb.2018.06.059.

[10] S. Acharya et al. "Investigations of Anisotropic Flow Using Multiparticle Azimuthal Correlations in pp, pPb, Xe-Xe, and Pb-Pb Collisions at the LHC". In: *Physical Review Letters* 123.14 (Oct. 2019). ISSN: 1079-7114. DOI: 10.1103/physrevlett.123.142301. URL: http://dx.doi.org/10.1103/PhysRevLett.123.142301.

[11] B. Alver et al. *The PHOBOS Glauber Monte Carlo.* 2008. arXiv: 0805.4411 [nucl-ex].

[12] S. Chatrchyan et al. "Study of high-p T charged particle suppression in PbPb compared to pp collisions at $\sqrt{s_{NN}}$ = 2.76 TeV". In: *The European Physical Journal C* 72.3 (Mar. 2012). ISSN: 1434-6052. DOI: 10.1140/epjc/s10052-012-1945-x. URL: http://dx.doi.org/10.1140/epjc/s10052-012-1945-x.

[13] K. Aamodt et al. "Suppression of charged particle production at large transverse momentum in central Pb–Pb collisions at $\sqrt{s_{NN}}$ = 2.76 TeV". In: *Physics Letters B* 696.1-2 (Jan. 2011), pp. 30–39. ISSN: 0370-2693. DOI: 10.1016/j.physletb.2010.12.020. URL: http://dx.doi.org/10.1016/j.physletb.2010.12.020.

[14] B. I. et al. Abelev. "Long range rapidity correlations and jet production in high energy nuclear collisions". In: *Phys. Rev. C* 80 (6 Dec. 2009), p. 064912. DOI: 10.1103/PhysRevC.80.064912. URL: https://link.aps.org/doi/10.1103/PhysRevC.80.064912.

[15] K. Aamodt et al. "Harmonic decomposition of two particle angular correlations in Pb–Pb collisions at $\sqrt{s_{\mathrm{NN}}}$ = 2.76 TeV". In: *Physics Letters B* 708.3-5 (Feb. 2012), pp. 249–264. ISSN: 0370-2693. DOI: 10.1016/j.physletb.2012.01.060. URL: http://dx.doi.org/10.1016/j.physletb.2012.01.060.

[16] Piotr Bożek and Wojciech Broniowski. "Charge Conservation and the Shape of the Ridge of Two-Particle Correlations in Relativistic Heavy-Ion Collisions". In: *Physical Review Letters* 109.6 (Aug. 2012). ISSN: 1079-7114. DOI: 10.1103/physrevlett.109.062301. URL: http://dx.doi.org/10.1103/PhysRevLett.109.062301.

[17] Steffen A. Bass, Pawel Danielewicz, and Scott Pratt. "Clocking Hadronization in Relativistic Heavy-Ion Collisions with Balance Functions". In: *Physical Review Letters* 85.13 (Sept. 2000), pp. 2689–2692. ISSN: 1079-7114. DOI: 10.1103/physrevlett.85.2689. URL: http://dx.doi.org/10.1103/PhysRevLett.85.2689.

[18] STAR Collaboration. "Narrowing of the Balance Function with Centrality in Au + Au Collisions at $\sqrt{s_{NN}}$ = 130 GeV". In: *Phys. Rev. Lett.* 90 (17 May 2003), p. 172301. DOI: 10.1103/PhysRevLett.90.172301. URL: https://link.aps.org/doi/10.1103/PhysRevLett.90.172301.

[19] Vardan Khachatryan et al. "Observation of long-range, near-side angular correlations in proton-proton collisions at the LHC". In: *Journal of High Energy Physics* 2010.9 (2010), p. 91.

[20] J. Adam et al. "Multiplicity and transverse momentum evolution of charge-dependent correlations in pp, p–Pb, and Pb–Pb collisions at the LHC". In: *The European Physical Journal C* 76.2 (Feb. 2016). ISSN: 1434-6052. DOI: 10.1140/epjc/s10052-016-3915-1. URL: http://dx.doi.org/10.1140/epjc/s10052-016-3915-1.

[21] Zhanna Khabanova. "Studies of collective effects in pp collisions at the LHC with the balance function for identified particles". PhD thesis. University Utrecht, 2020.

[22] *LHC Facts and Figures*. URL: https://home.cern/resources/brochure/knowledge-sharing/lhc-facts-and-figures. (accessed: 19-10-2020).

[23] The ALICE Collaboration. "The ALICE experiment at the CERN LHC". In: *Journal of Instrumentation* 3.08 (Aug. 2008), S08002–S08002. DOI: 10.1088/1748-0221/3/08/s08002. URL: https://doi.org/10.1088%2F1748-0221%2F3%2F08%2Fs08002.

[24] Sergei A. Voloshin. "Two particle rapidity, transverse momentum, and azimuthal correlations in relativistic nuclear collisions and transverse radial expansion". In: *Nuclear Physics A* 749 (Mar. 2005), pp. 287–290. ISSN: 0375-9474. DOI: 10.1016/j.nuclphysa.2004.12.053. URL: http://dx.doi.org/10.1016/j.nuclphysa.2004.12.053.

[25] B. Abelev et al. "Charge correlations using the balance function in Pb–Pb collisions at $\sqrt{s_{NN}}$ =2.76 TeV". In: *Physics Letters B* 723.4-5 (June 2013), pp. 267–279. ISSN: 0370-2693. DOI: 10.1016/j.physletb.2013.05.039. URL: http://dx.doi.org/10.1016/j.physletb.2013.05.039.

[26] *AOD filter bits*. URL: https://twiki.cern.ch/twiki/pub/ALICE/PWGPPAODTrackCuts/rs_aodbits_130214_copy.pdf. (last updated: 13-04-2014).

[27] Xin-Nian Wang and Miklos Gyulassy. "hijing: A Monte Carlo model for multiple jet production in pp, pA, and AA collisions". In: *Phys. Rev. D* 44 (11 Dec. 1991), pp. 3501–3516. DOI: 10.1103/PhysRevD.44.3501. URL: https://link.aps.org/doi/10.1103/PhysRevD.44.3501.

[28] Rene Brun et al. *GEANT: detector description and simulation tool*. Tech. rep. CERN, 1993.

[29] Michael L. Miller et al. "Glauber modeling in high energy nuclear collisions". In: *Ann. Rev. Nucl. Part. Sci.* 57 (2007), pp. 205–243. DOI: 10.1146/annurev.nucl.57.090506.123020. arXiv: nucl-ex/0701025.

[30] "Centrality determination using the Glauber model in Xe-Xe collisions at $\sqrt{s_{\mathrm{NN}}}$ = 5.44 TeV". In: (Apr. 2018). URL: http://cds.cern.ch/record/2315401.

[31] J. Adam et al. "Centrality dependence of particle production in pPb collisions at $\sqrt{s_{\mathrm{NN}}}$ = 5.02 TeV". In: *Physical Review C* 91.6 (June 2015). ISSN: 1089-490X. DOI: 10.1103/physrevc.91.064905. URL: http://dx.doi.org/10.1103/PhysRevC.91.064905.

[32] P. Möller et al. "Nuclear ground-state masses and deformations: FRDM(2012)". In: *Atomic Data and Nuclear Data Tables* 109-110 (May 2016), pp. 1–204. ISSN: 0092-640X. DOI: `10.1016/j.adt.2015.10.002`. URL: `http://dx.doi.org/10.1016/j.adt.2015.10.002`.

[33] Giuliano Giacalone et al. "Hydrodynamic predictions for 5.44 TeV Xe+Xe collisions". In: *Physical Review C* 97.3 (Mar. 2018). ISSN: 2469-9993. DOI: `10.1103/physrevc.97.034904`. URL: `http://dx.doi.org/10.1103/PhysRevC.97.034904`.

[34] Sangyong Jeon and Scott Pratt. "Balance functions, correlations, charge fluctuations, and interferometry". In: *Phys. Rev. C* 65 (4 Apr. 2002), p. 044902. DOI: `10.1103/PhysRevC.65.044902`. URL: `https://link.aps.org/doi/10.1103/PhysRevC.65.044902`.

[35] B. Andersson et al. "Parton fragmentation and string dynamics". In: *Physics Reports* 97.2 (1983), pp. 31–145. ISSN: 0370-1573. DOI: `https://doi.org/10.1016/0370-1573(83)90080-7`. URL: `http://www.sciencedirect.com/science/article/pii/0370157383900807`.

[36] K.J Eskola, K Kajantie, and J Lindfors. "Quark and gluon production in high energy nucleus-nucleus collisions". In: *Nuclear Physics B* 323.1 (1989), pp. 37–52. ISSN: 0550-3213. DOI: `https://doi.org/10.1016/0550-3213(89)90586-5`. URL: `http://www.sciencedirect.com/science/article/pii/0550321389905865`.

[37] Jinjin Pan. "Balance functions of (un)identified hadrons in Pb–Pb, p–Pb, and pp collisions at the LHC". In: *Nucl. Phys. A* 982 (2019). Ed. by Federico Antinori et al., pp. 315–318. DOI: `10.1016/j.nuclphysa.2018.09.022`. arXiv: `1807.10377 [nucl-ex]`.

[38] T. Pierog et al. "EPOS LHC: Test of collective hadronization with data measured at the CERN Large Hadron Collider". In: *Physical Review C* 92.3 (Sept. 2015). ISSN: 1089-490X. DOI: `10.1103/physrevc.92.034906`. URL: `http://dx.doi.org/10.1103/PhysRevC.92.034906`.

[39] S. Acharya et al. "Centrality and pseudorapidity dependence of the charged-particle multiplicity density in Xe–Xe collisions at $\sqrt{s_{NN}} = 5.44$ TeV". In: *Physics Letters B* 790 (Mar. 2019), pp. 35–48. ISSN: 0370-2693. DOI: `10.1016/j.physletb.2018.12.048`. URL: `http://dx.doi.org/10.1016/j.physletb.2018.12.048`.

[40] Scott Pratt. "General charge balance functions: A tool for studying the chemical evolution of the quark-gluon plasma". In: *Physical Review C* 85.1 (Jan. 2012). ISSN: 1089-490X. DOI: `10.1103/physrevc.85.014904`. URL: `http://dx.doi.org/10.1103/PhysRevC.85.014904`.
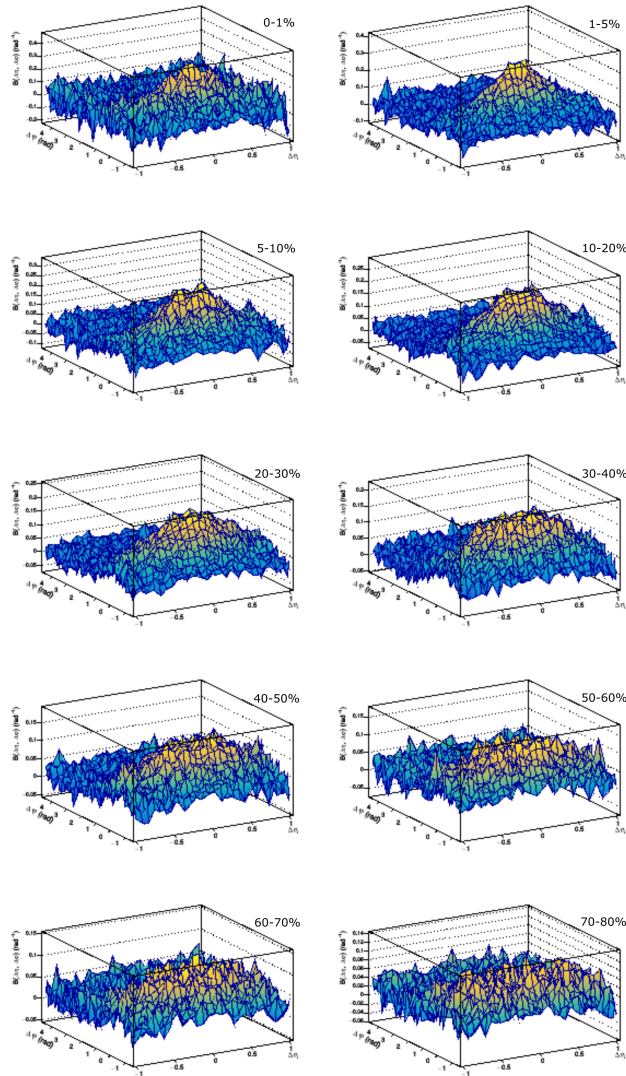
Appendix A

Additional figures

Figure A1: The balance function for multiplicities 0-1%, 1-5%, 5-10%, 10-20%, 20-30%, 30-40%, 40-50%, 50-60%, 60-70% and 70-80%, respectively.
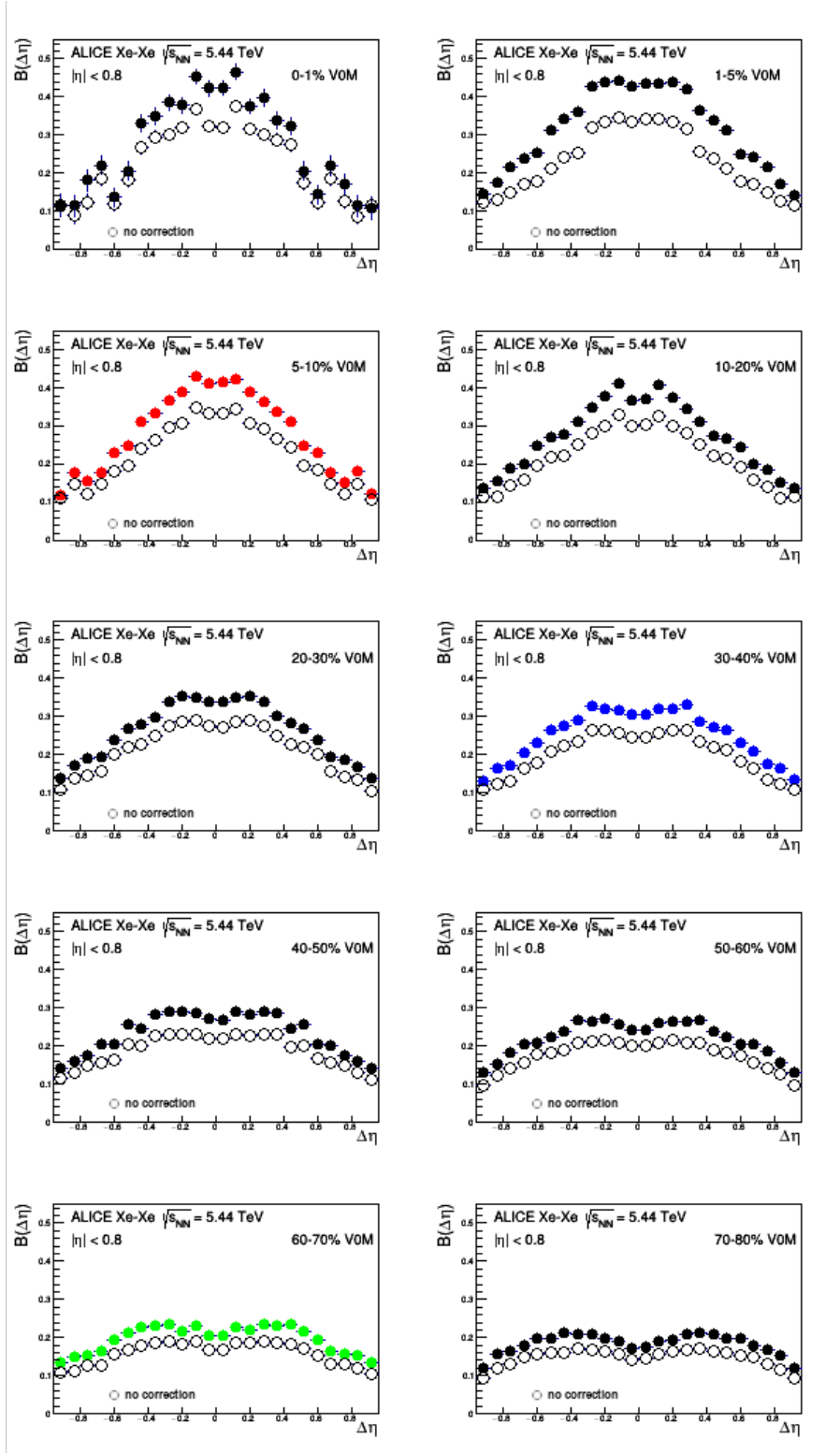
Figure A2: Projections of the balance function in $\Delta\eta$, on the near-side ($-\pi/2 < \Delta\varphi < \pi/2$), for multiplicities 0-1%, 1-5%, 5-10%, 10-20%, 20-30%, 30-40%, 40-50%, 50-60%, 60-70% and 70-80%, respectively. The colored projections correspond to the projections in Figure 6.2a. The open circles represent the projections without applying corrections.
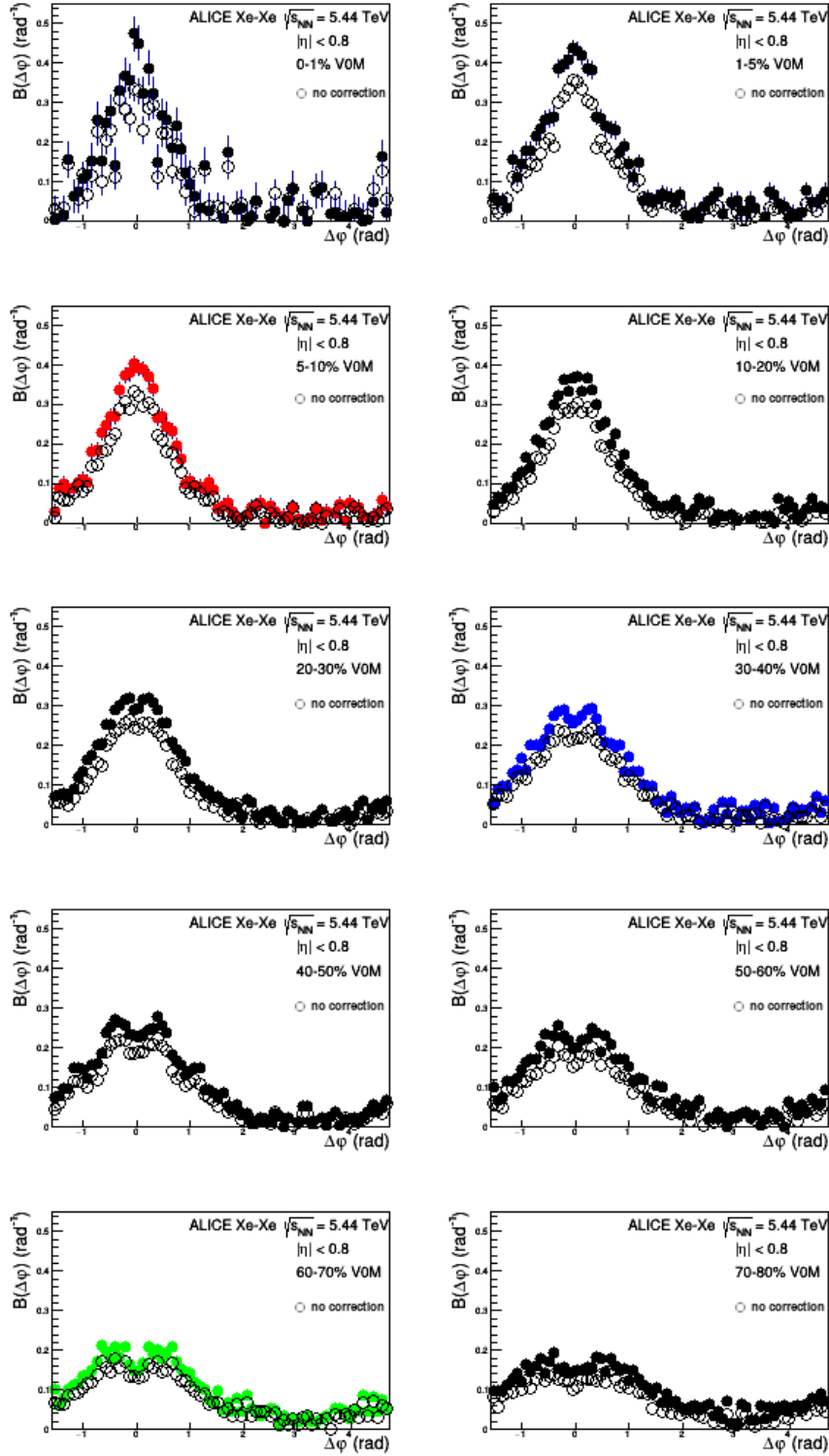
Figure A3: Projections of the balance function in $\Delta\eta$, on the near-side $(-\pi/2 < \Delta\varphi < \pi/2)$, for multiplicities 0-1%, 1-5%, 5-10%, 10-20%, 20-30%, 30-40%, 40-50%, 50-60%, 60-70% and 70-80%, respectively. The colored projections correspond to the projections in Figure 6.2b. The open circles represent the projections without applying corrections.